A CA1 circuit motif that signals the start of information integration

Raphael Heldman[1], Dongyan Pang[1], Xiaoliang Zhao[1], Yingxue Wang[1]

[1]Max Planck Florida Institute for Neuroscience, One Max Planck Way, Jupiter, FL 33458, USA

Correspondence: Yingxue.Wang@mpfi.org

Abstract

Integrating information from the recent past is critical for guiding predictions and shaping behavior. The process of integrating information, such as tracking distance traveled or time elapsed, begins with establishing a starting point. Yet, the mechanisms by which neural circuits utilize relevant cues to initiate integration remain unknown. Our study sheds light on this question by identifying a subpopulation of CA1 pyramidal neurons called PyrDown. These neurons shut down their activity at the beginning of distance or time integration and then gradually ramp up their firing as the animal approaches the reward. PyrDown neurons provide a mechanism for representing integrated information through ramping activity, complementing the well-known place/time cells that respond to specific distances or time points. Our findings also reveal that parvalbumin inhibitory interneurons mediate the shutdown of PyrDown neurons, uncovering a circuit motif that enables the initiation of subsequent information integration to improve future predictions.

Introduction

Imagine walking in the evening from your home to a nearby park. In the dark, you can rely on your estimate of distance to predict your location, but you may also occasionally look around and use available landmarks to update your position. These landmarks help to reset your current estimate and start a new distance counting, leading to a more accurate predictions of future locations. Hippocampal circuits play a crucial role in integrating self-motion information to compute distance relative to external cues, a process known as path integration(McNaughton et al., 2006, 1996). Yet, it remains unknown how these circuits start a new integration by selectively responding to salient cues, thereby guiding future predictions.

In the hippocampal CA1 region, some pyramidal neurons display activation at specific distances or time points even when sensory cues are suppressed or absent. It occurs, for example, when a rodent is trained to run on a wheel or treadmill while performing a memory task. The activity of these neurons collectively forms a sequence that spans the entire running period and encodes distance or time accumulated during the run. These sequential activity patterns, generated in the absence of the ever-changing external sensory inputs, are referred to as internally generated sequences (IGSs)(Kraus et al., 2013; MacDonald et al., 2013, 2011; Pastalkova et al., 2008; Taxidis et al., 2020; Wang et al., 2015).

Previous evidence suggests that either sensory(Modi et al., 2014; Taxidis et al., 2020) or motor cues(Villette et al., 2015) can initiate IGSs, which likely encode the integrated distance or time interval starting from these cues. This implies that CA1 neurons can utilize these cues to start integration. Yet, how the CA1 circuits perform computations to signal and initiate the integration remains unknown.

Here, we interrogated the neuronal dynamics of all pyramidal neurons recorded in the CA1 region, not just the subset involved in IGSs. Our focus was on the dynamics surrounding the moment when the animal begins to integrate over distance or time. We also examined the contribution of fast-spiking Parvalbumin-positive (PV) inhibitory interneurons to the observed neuronal dynamics and their potential role in signaling the start of integration. Our study reveals a circuit-level computation performed by the hippocampus to initiate moment-to-moment information integration during experience encoding.

Results

A simple behavioral task that generates IGSs

We developed virtual reality (VR) setups (Figure 1A) to precisely control the timing and spatial location of visual stimuli presented to a mouse that is running on a treadmill while being head-fixed. Using these setups, we designed two behavioral paradigms – a passive task and an active task.

The passive task, which is a non-memory task, starts with a gray-colored screen. The animal is required to run for 180 cm while this visual stimulus stays constant (referred to as the cue-constant segment). A drop of water reward is then automatically delivered at 180 cm (Figure 1B top; STAR methods). This passive task serves as a baseline control to replicate previously reported non-memory tasks(Hirase et al., 1999; Pastalkova et al., 2008). As trained animals performed this task, they showed a stereotypical running speed profile, and licks occurred sparsely before reward delivery (Figure 1C top; Figures 1D and 1E). During extracellular recording in the hippocampal CA1 region using silicon probes, pyramidal neurons tended to fire throughout the 180 cm cue-constant segment (Figure 1F left). Neurons rarely developed tuning to a particular running distance within the cue-constant segment, meaning that the neuronal firing field produced by internal computations -- internally generated field (IGF) was absent in this task (Figure 1H).

The active task is a variant of the passive task that requires a higher level of cognitive demand. In this task, a brief visual cue marks the start of a trial, and the animal is then required to run for 180 cm while the gray-colored screen stays constant. To trigger a water reward, the animal must lick within a 40 cm reward zone. Failing to lick within the reward zone will result in no water reward (Figure 1B bottom; STAR methods). This task requires the animal to accumulate distance over the cue-constant segment to predict the upcoming reward.

Trained animals showed stereotypical licking and running speed profiles (Figure 1C bottom; Figures 1D and 1E). When selecting sessions in which the mean running speed during the cue-constant segment did not significantly differ from the passive task (Figure

1D; STAR methods, Passive: mean±SEM = 34.41±1.80 cm/s, Active: 34.73±1.23 cm/s, p=0.63, rank-sum test. Mean±SEM and rank-sum test are used if not specifically stated), we observed a significant increase in predictive licks before reward delivery (Figure 1E, mean licks per 1 cm bin between 100-180 cm, PL: 0.083±0.025, AL: 0.17±0.022, p=0.012). The ability to perform this active task required an intact hippocampus (Figures S1A-S1D).

To perform the active task correctly, the animal must reset its distance counter at the beginning of each trial. Its stereotypical trial-by-trial behavior (Figure 1C bottom) implies that it can detect the start and end of a trial.

In CA1 extracellular recordings taken during the active task, pyramidal neurons displayed significantly higher trial-by-trial correlation than those in the passive task (Figure 1G, mean activity correlation over trials, Passive: 0.006±7.9e-04, Active: 0.033±5.2e-4). Pyramidal neurons with IGFs were present (Figures 1F right and 1H, 4.30±0.58% neurons; STAR methods). These neurons together formed a sequence that covered the 180 cm cue-constant segment, constituting an IGS (Figure 2B).

The IGFs were preferentially activated at specific distances during the cue-constant segment in each trial, and similar IGSs were initiated every trial (Figures 1F and 2A), suggesting that CA1 neurons can encode distance relative to the start of each trial.

The initiation of an IGS aligns to the running onset

The fact that similar IGSs were initiated at the beginning of each trial prompted us to ask what salient cue may trigger their initiation and serve as the starting point of integration over distance. We judged the two sensory cues available in the trial structure of the active task: the onset of the visual cue at the trial's beginning and the reward delivery (Figure 2C). To reveal the temporal relationship between these sensory cues and the neuronal activity, we aligned neurons' spiking activity within each trial to either cue onset or reward and plotted them against time instead of distance. However, the spikes failed to align well with either cue (Figure 2E left column; Figure S1E). Hence, CA1 neurons must respond to some other salient signal to initiate IGSs.

We found that animals' running onset did not align with the visual cue at the trial's start when plotting their run speed over time (instead of distance) (Figure 2D). This result made us question whether the run onset serves as a salient cue to initiate IGSs.

To determine the run onset in each trial, we identified the time when the animal first started running after it had travelled 180 cm in the cue-constant segment of the previous trial (STAR methods). We then adjusted each trial's start to be the run onset, as opposed to cue onset (Figure 2E right column; Figure S1E). After aligning neuronal activity to run onset, more neurons displayed IGFs (Figure 2J, 9.46±0.72% neurons; STAR methods) by responding consistently at specific time points. These neurons also exhibited improved trial-by-trial activity correlation (Figure 2G, cue onset: 0.14±0.0035, run onset: 0.20±0.0037) and spatial information (Figure 2H, cue onset: 0.29±0.0077bits/s, run onset: 0.34±0.0091bits/s). They consistently advanced their spike phases in relation to the ongoing theta oscillations, a phenomenon known as phase precession, which is a key characteristic of place cells(O'Keefe and Recce, 1993; Skaggs et al., 1996) and cells with IGFs(Pastalkova et al., 2008) (Figures S1F and S1G). On the population level, IGSs also

became significantly sharper (Figures 2F and 2I, population correlation: cue onset: 0.20±0.0086, run onset: 0.24±0.0076).

Interestingly, the improvement in trial-by-trial correlation was not limited to the small subset of neurons with IGFs, but was also observed when considering all recorded pyramidal neurons (Figures S1H and S1I). Additionally, this improvement was not caused by a sudden transition in the brain state, which typically happens when an animal starts running after a period of immobility(Schultheiss et al., 2020). In the active task, the brain state during the short pauses for reward consumption (with an average pause time of 1.88s between reward delivery and the next run onset) was not different from when the animals were running slowly (speed 5-20 cm/s, Figures S1J and S1K). Overall, the run onset may act as a salient cue to start the integration over distance in this task. However, it was challenging to distinguish whether animals integrated over distance or time due to their stereotypical running speed profiles.

To further probe whether proper run onset improves the animals' ability to integrate over distance, we designated "good" trials based on the following criteria: 1) The animal came to a complete stop just before the run onset (speed < 1 cm/s; STAR methods). 2) The subsequent running was mostly continuous, with a total stop time shorter than 2s after run onset. 3) The animal accurately located the reward zone and successfully obtained reward in the previous trial. Compared to good trials (77.90±2.88%), in trials that failed these criteria ("bad trials"), the animals licked more randomly and at earlier times (Figures 2K and S1L, mean number of licks per bin: good trials: 0.011±0.0024, bad trials: 0.027±0.0063) and stopped for longer periods between run onset and the trial's end (Figure 2M, good trials: 0.41±0.010s, bad trials: 5.85±0.73s). However, the mean speed was not different (Figures 2L and S1M, good trials: 48.12±0.84cm/s, bad trials: 45.20±0.84cm/s). Starting to lick earlier can prevent missing rewards, even if the animals were not accurately measuring distance. Nevertheless, the percentage of rewarded trials was lower (Figure S1N).

Next, we examined whether the expression of firing fields requires a proper run onset. The IGFs in bad trials were less correlated than in good trials (Figure 2N, good trials: 0.22±0.0035, bad trials: 0.12±0.0066), and the IGSs were impaired (Figures 2O and S1O). This evidence at both the behavioral and neuronal levels suggested that run onset likely served as a start signal to facilitate subsequent distance encoding.

Subpopulations of pyramidal neurons display distinct responses around run onset

Building upon the observed improvement in trial-by-trial activity correlation in all recorded CA1 pyramidal neurons after aligning to the run onset, we extended our examination beyond the small subset of neurons with IGFs and investigated the neuronal dynamics of all CA1 pyramidal neurons around run onset (7114 neurons, 28 animals, including neurons with IGFs (650 neurons)). To characterize the change in each neuron's activity around run onset, we first calculated the ratio of the mean firing rate immediately following and preceding the run onset (FR_{aft}/FR_{bef}) (Figure 3A).

Arranging all recorded neurons based on their FR_{aft}/FR_{bef} revealed subpopulations with distinct patterns (Figure 3A). 37.2% of neurons showed low firing rate prior to run onset,

followed by a rapid increase thereafter (designated as "PyrUp" (Figures 3B-3D, and S2A, neurons with $FR_{aft}/FR_{bef} > 3/2$, the presence of PyrUp was not sensitive to the threshold value). In contrast, 19.4% of neurons displayed elevated firing before run onset and became suppressed thereafter (designated as “PyrDown" (Figures 3E-3G, and S2A, neurons with $FR_{aft}/FR_{bef} < 2/3$). The remaining neurons exhibited no significant changes in firing rate (designated as “PyrOther” neurons, Figures S2G1-S2G3).

To avoid bias in grouping neurons, we only included neurons whose FR_{aft}/FR_{bef} differed significantly from shuffled data and obtained similar results (Figures S2I-S2K; STAR methods). Likewise, only examining pyramidal neurons with IGFs (9.46±0.72% neurons) still yielded matching populations of PyrUp and PyrDown neurons (Figures S2B-S2F), demonstrating the robustness of our findings across different neuron subgroups.

To examine whether the PyrUp and PyrDown neurons belong to distinct cell types, we assessed their relative depths to the center of the CA1 pyramidal layer as determined by local field potential signatures(Mizuseki et al., 2011), and observed no significant difference (Figure S2H). This implies that each subpopulation contains a combination of both deep and superficial cells in relation to the pyramidal layer center(Cembrowski et al., 2016; Danielson et al., 2016; Mizuseki et al., 2011; Slomianka et al., 2011; Soltesz and Losonczy, 2018). To further determine whether they form functionally distinct clusters, we applied t-distributed stochastic neighbor embedding (t-SNE)(Maaten and Hinton, 2008) on the mean firing rate profiles from all pyramidal neurons around run onset (Figure 3H). Our results showed that PyrUp and PyrDown neurons were situated around opposite ends of a continuous cluster, instead of forming separate clusters, suggesting that these two subpopulations are part of the same pyramidal population with a continuous spectrum of firing rate changes around run onset.

We then probed whether the observed changes in firing rate were dependent on a proper run onset. In good trials, the firing rate change at run onset was significantly higher for both PyrUp and PyrDown populations compared to bad trials (Figures 3B, 3C, 3E, and 3F, relative FR change: PyrUp: good trials: 0.45±0.0036, bad trials: 0.20±0.012, PyrDown: good trials: -0.41±0.0048, bad trials: -0.13±0.020). However, there was no significant difference in the mean firing rates between good and bad trials (Figures 3D and 3G, PyrUp: good trials: 1.76±0.032Hz, bad trials: 1.72±0.061Hz, PyrDown: good trials: 1.49±0.042Hz, bad trials: 1.50±0.087Hz). A separate examination of neurons with IGFs produced similar results. Thus, the activity patterns of PyrUp and PyrDown neurons preferentially occur in trials properly delineated by run onset and exhibited good performance.

Subpopulations of pyramidal neurons respond specifically as integration starts

PyrUp and PyrDown neurons’ firing rate changes around run onset made us ask if they responded specifically to the run onset around trial’s start or simply to any instance of running onset. To answer this question, we identified spontaneous stops that occurred during a trial (19 animals, 32 sessions, 2902 neurons; STAR methods). The averaged responses of PyrUp and PyrDown neurons at the onset of running immediately after each spontaneous stop (“spontaneous run onset”) were strongly attenuated relative to the run onset at trial’s start (Figures 3I, 3J, 3L, and 3M, relative FR change: PyrUp: at

spontaneous run onset: 0.10±0.008, at trial run onset: 0.33±0.0069, PyrDown: at spontaneous run onset: -0.065±0.018, at trial run onset: -0.40±0.012), without a change in mean firing rate (Figures 3K and 3N, PyrUp: at spontaneous run onset: 2.12±0.06Hz, at trial run onset: 2.11±0.06Hz, PyrDown: at spontaneous run onset: 1.70±0.088Hz, at trial run onset: 1.72±0.094Hz). Our results remained consistent when selecting recording sessions with matching speed during both spontaneous running and running at trial's start (Figure S3A, 13 animals, 21 sessions, 1731 neurons; STAR methods). This suggests that the responses of PyrUp and PyrDown neurons are influenced by context rather than simply by the onset of locomotion. We further selected pyramidal neurons with significantly increased or decreased FR_{aft}/FR_{bef} compared to shuffled data after aligning spikes to the spontaneous run onset ("PyrUp-Spon" or "PyrDown-Spon", Figures S3B and S3C; STAR methods). These neurons exhibited attenuated response around the run onset at trial's start (subsequently referred to as "run onset", Figure S3D). Hence, instead of simply reacting to the onset of running, PyrUp and PyrDown neurons respond specifically around the beginning of each trial when the animal likely starts counting distance or time.

To examine if the responses of PyrUp and PyrDown neurons are specific to a task that require the animals to integrate over distance or time, we analyzed recordings from the passive task in which distance counting is not required. There, a much lower percentage of pyramidal neurons exhibited a significantly reduced FR_{aft}/FR_{bef} than shuffled data ("PyrDown-Pass") compared to the active task (Figure 3P, PyrDown-Pass: 3.03±1.45%, PyrDown: 13.03±0.79%). This percentage remained low after selecting sessions with matching running speed in both the passive and active tasks (Figures S3E, S3F, and S3H). In contrast, the percentage of neurons with a significantly increased FR_{aft}/FR_{bef} than shuffled data ("PyrUp-Pass") did not change (Figures 3O and S3G, PyrUp-Pass: 35.49±8.16%, PyrUp: 41.13±0.97%). Together, these results suggest that a greater proportion of CA1 pyramidal neurons are prone to shut down their activity around run onset when it marks the start of integration over distance or time.

To investigate whether the shutdown of PyrDown may act as a general starting mechanism independent of run onset, we designed an immobile version of the active task. In this version, the animal was confined within a tube(Guo et al., 2014) and following a brief visual cue, was required to estimate the passage of a 4-second time period while the gray-colored screen stays constant and to lick within a 1.5-second reward zone to trigger reward delivery (Figure S3I; STAR methods). Aligning the neuronal activity to available sensory or motor cues in the task, we found the neuronal activity was better aligned to the last lick of the previous trial instead of the start cue onset or reward (5 animals, 15 sessions, 748 neurons). IGSs were present after this alignment (Figure S3J, 6.72±1.56% neurons), supporting that the requirement of integration over time instead of distance can also lead to the expression of IGSs.

After aligning to the last lick, a higher percentage of pyramidal neurons displayed a significantly increased or decreased FR_{aft}/FR_{bef} than shuffled data ("PyrUp-Imm" and "PyrDown-Imm") compared to the active task (Figures S3K-S3O). Together, these results suggest that the trial start signal is not restricted to the onset of locomotion, and that the shutdown of PyrDown neurons may be a general mechanism for initiating integration of

either distance or time during distinct behavioral states, including locomotion and immobility.

Parvalbumin-positive basket cells display ramping activity around run onset

The distinct firing patterns of PyrUp and PyrDown neurons around run onset in the active task prompted us to question how the CA1 circuit produces such responses. Here, we sought to examine the role of CA1 inhibitory neurons in regulating neuronal activity around run onset. Since parvalbumin-positive (PV) basket cells exert direct perisomatic inhibition onto pyramidal neurons, and can efficiently control their spike timing and synchrony(Freund and Katona, 2007; Klausberger, 2009; Korotkova et al., 2010), we posited that they are good candidates to control the responses of PyrUp and PyrDown neurons at run onset.

To identify PV-basket cells, we started by separating putative inhibitory neurons based on their spike waveforms and auto-correlograms(Stark et al., 2013). Then, using the spike auto-correlograms, spike theta phase histograms(Klausberger and Somogyi, 2008), and their relative depths to the center of the CA1 pyramidal layer(Klausberger and Somogyi, 2008), we classified these neurons into clusters. Among the six resulting clusters, we identified one as the putative PV-basket cells (Figures 4A-4C; green dots in Figures 4E and S3Q (3D view); Figures S3S and S3U; STAR methods). Most of the neurons in this cluster showed a clear increase in firing rate around run onset (designated as “PV-Up”, 75/114 neurons, Figures 4F and 4G).

To verify the identity of these putative PV-basket cells, we performed optogenetic tagging by transfecting the CA1 PV-expressing interneurons with channelrhodopsin-2 (ChR2) in PV-Cre animals (Figures 4D and S3P; 7 animals). The tagged neurons overlapped with multiple clusters in Figure 4E, supporting the previous findings that PV interneurons contain multiple cell types(Klausberger and Somogyi, 2008). However, a large proportion of the tagged neurons belonged to the putative PV-basket cell cluster (13/30 neurons) and showed similar auto-correlograms and theta phase histograms (Figures S3S-S3V). Most of the tagged PV-basket cells (10/13 neurons) also showed a clear increase in their firing rate around run onset (Figures 4H, 4I, and S3R). In bad trials, the firing rate increase of the PV-Up neurons was weakened, despite the mean firing rate remaining unchanged (Figures 4G, 4J, and 4K, relative FR change: good trials: 0.33±0.012, bad trials: 0.16±0.021, mean FR: good trials: 20.16±1.29Hz, bad trials: 18.27±2.15Hz), suggesting proper run onset is required for the observed firing rate increase.

We further investigated the temporal relationship between the responses of PV-Up interneurons and PyrUp and PyrDown neurons. The normalized average firing rate profiles of PV-Up and PyrUp neurons showed a concurrent increase in their firing rate around run onset, with PV-Up neurons leading PyrUp neurons (Figure 4L left, time reaching 90% from minimum to maximum firing rate within [-1 1.5]s window: PyrUp: 0.77±0.01s, PV-Up: 0.50±0.04s, p = 7.53e-09). In contrast, PyrDown neurons started to decrease their activity after the activity increase of PV-Up neurons and reached minimum after the peak activity of PV-Up neurons (Figure 4L right, time reaching 90% from maximum to minimum firing rate within [-1 1.5]s window: PyrDown: 0.60±0.01s, p = 6.62e-

04 compared with PV-Up). Thus, functionally, PV-basket cells appear to preferentially inhibit PyrDown neurons while only weakly impacting PyrUp neurons.

Parvalbumin-positive interneurons are necessary to start distance counting at run onset

To determine if PV interneurons evoke stronger inhibition on PyrDown neurons than PyrUp neurons, we conducted an experiment silencing CA1 PV interneurons and observed the impact on PyrDown and PyrUp neurons. We utilized soma-targeted anion-conducting channelrhodopsins (stGtACR2) to hyperpolarize CA1 PV cells with 450 nm light illumination(Mahn et al., 2018), and recorded the neuronal activity unilaterally from dorsal CA1 using an optrode (Figure 5A top). In a subset of trials, we silenced PV interneurons for 3 seconds immediately after run onset (Figure 5A bottom), which resulted in clear silencing of some putative PV basket cells (Figures S 4A and S4B). Please note that the starting time of the closed-loop optogenetic stimulation was slightly delayed compared to the run onset identified during data analysis (0s in Figure 5B; STAR methods). Silencing PV cells primarily impacted PyrDown neurons, causing a significant elevation in their firing rate after run onset (Figures 5B and S4C, and 5G-5J, 3 animals, 64/335 neurons, relative FR change: control: -0.39±0.021, stimulation: -0.16±0.043). Conversely, PyrUp neurons did not display a significant change in their firing rate (Figures 5C-5F, 139/335 neurons, relative FR change: control: 0.45±0.017, stimulation: 0.40±0.024).

This manipulation did not affect neurons with IGFs, with neither PyrUp (31/49 neurons) nor PyrDown group (13/49 neurons) showing significant changes in firing rate (Figures 5K-5S, relative FR change: PyrUp: control: 0.59±0.040, stimulation: 0.58±0.048, PyrDown: control: -0.37±0.053, stimulation: -0.30±0.11). Furthermore, there was no difference in the neuronal activity correlation or the number of neurons with IGFs between the stimulation and control trials (Figures S4D and S4E).

To assess the impact of selectively manipulating PyrDown neuron activity after run onset on behavior, we silenced PV interneurons bilaterally using the same stimulation protocol in a separate cohort of animals (Figure 5T). Results showed a significant increase in early licks within 100 cm after run onset (Figures 5U and 5V, control: 0.022±0.0093, stimulation: 0.060±0.018), with an unchanged licking pattern after 100 cm (Figures S4F and S4H-S4J). That is, this effect was mostly confined to shortly after run onset. In addition, although the percentage of trials in which animals stopped after run onset remained unchanged (Figure S4G), the amount of time they stopped increased significantly (Figure 5W, control: 0.11±0.060s, stimulation: 0.39±0.082s). Mean speed was not altered, indicating unimpaired locomotion (Figure 5X, control: 60.40±2.42cm/s, stimulation: 56.87±2.14cm/s). The percentage of rewarded trials also did not differ (Figure 5Y, control: 100.00±0.00%, stimulation: 99±0.56%).

As a control, in some recording sessions, the optogenetics patch cables were only loosely mated with the implanted fiber optic cannulas, preventing light from propagating into CA1. During these sessions, animals exhibited normal behavior, suggesting that the laser light alone is unlikely to affect behavior (Figures S6H-S6L; STAR methods).

As the PV interneurons' activity began ramping up before run onset, to examine the effect of silencing PV interneurons during the ramp-up period on PyrDown neurons, we inactivated PV cells for 3 seconds starting from reward delivery in the previous trial to cover the ramp-up period (Figure S4K). The results confirmed that silencing the PV ramp was necessary to specifically shut down PyrDown neurons around run onset (Figures S4L-S4O).

In the same cohort of animals from Figure 5T, bilateral optogenetic manipulation after reward delivery caused similar behavioral impairment as inactivating after run onset (Figures S4P-S4T). Despite an increase in early licks within 100 cm after run onset (Figures S4Q and S4R), the total licking count from reward delivery to trial's end was unchanged (control: 69.60±8.23, stimulation: 60.99±6.71, $p = 0.48$). This suggests that PV inactivation did not simply enhance the animals' propensity to lick. Additionally, we observed a strong tendency for animals to stop during the initial 100 cm of the run (Figure S4U).

The observed behavioral impairment primarily occurring shortly after run onset suggests a difficulty in accurately locating the start in each trial. We posit that PV interneurons are necessary for shutting down PyrDown neurons at run onset, and for demarcating individual trials and initiating integration over distance or time at the beginning of each trial.

Activating parvalbumin-positive interneurons at run onset does not affect behavior

We hypothesized that correct initiation of the integration over distance or time requires the shutdown of PyrDown neurons at run onset. Given the limited potential for improvement in task performance, we anticipate that strengthening this shutdown should not negatively impact the trained behavior.

As PyrUp and PyrDown neurons are composed of a mixed population of pyramidal cell types, it is not feasible to specifically manipulate either population through a cell-type-specific approach. Instead, we attempted to enhance the run-onset shutdown of PyrDown neurons by optogenetically activating PV interneurons (Figure 6A). As shown in Figures 6B-6E, a 0.5s activation of PV interneurons at run onset sharpened the shutdown of PyrDown neurons (mean FR 0 to 1s: control: 1.41±0.16Hz, stimulation: 1.09±0.13Hz). However, this manipulation also significantly reduced the firing rate of PyrUp (Figures 6B and 6C, mean FR 0 to 1s: control: 2.33±0.17Hz, stimulation: 1.49±0.12Hz) and PyrOther neurons (Figure S5D, mean FR 0 to 1s: control: 2.34±0.17Hz, stimulation: 1.67±0.12Hz). Neurons with IGFs slightly decreased their firing rate after run onset as well (Figures S5A-S5C, and S5E).

To determine the impact of this manipulation on behavior, we conducted a separate experiment where we activated PV interneurons bilaterally immediately after run onset in a different cohort of animals. Our results showed that inactivating pyramidal neurons at run onset had minimal impact on task performance, even with a 1.5s stimulation (Figures 6F-6J, initial tests with a 0.5s stimulation induced no discernible behavioral change). This manipulation caused no significant changes in speed, licking pattern, or stop time from the run onset to the trial's end (Figures 6G-5I, and S5K-S5L, number of licks /bin (30-100

cm): control: 0.023±0.0063, stimulation: 0.069±0.021, total stop time: control: 0.12±0.078s, stimulation: 0.19±0.077s). The percentage of rewarded trials only declined slightly (Figure 6J, control: 100.00±0.00%, stimulation: 99.47±0.38%).

Therefore, the shutdown of PyrDown activity at run onset (through activating PV interneurons) may contribute to starting the integration and maintaining task performance, despite the simultaneous inactivation of PyrUp and PyrOther activity.

PyrDown neurons' slow ramping activity during the cue-constant segment is necessary for task performance

The shutdown of PyrDown neuron activity at run onset may allow for a gradual ramp-up during the cue-constant segment as the animal approached the reward zone. This ramp-up may contain information about distance traveled or time passed since run onset, or it may serve as a predictor of the upcoming reward. To explore the first possibility, we applied Bayesian decoding(Mau et al., 2018) to the activity patterns of PyrDown neurons without IGFs in each recording and demonstrated that the passage of time after run onset was correctly decoded (Figures S6A-S6C).

To probe whether PyrDown neurons play a role in encoding reward or reward prediction, we aligned the trial-by-trial activity to run onset, the first lick of each trial, and reward delivery, respectively. Our analysis revealed neurons that were significantly tuned to each of these features compared to shuffled data (Figure S6F). The proportion of PyrDown neurons tuned to the start of predictive licking was 8%, and to reward was 15%, whereas only 3% and 1% of PyrUp neurons showed such tuning (Figure S6G).

To examine whether the gradual ramp-up activity of PyrDown neurons is required to maintain task performance, we activated PV interneurons around the location where the activity of PyrDown neurons was gradually ramping up while the activity of PyrUp neurons was declining (after 120 cm of running during the cue-constant segment, Figure 6K). This manipulation significantly reduced the ramp-up activity of PyrDown neurons around the end of the cue-constant segment (Figures 6N and 6O, mean FR 3 to 4s: control: 1.41±0.19Hz, stimulation: 0.72±0.14Hz) but also lowered the activity of other neurons (Figures 6L, 6M, and S5F-S5J, mean FR 3 to 4s: PyrUp: control: 1.15±0.098Hz, stimulation: 0.50±0.045Hz).

To assess the impact on behavior, we performed bilateral optogenetic manipulation in the same cohort of animals as in Figure 6F (Figure 6P), and observed clearly impaired task performance (Figures 6Q-6T, number of licks /bin (30-100 cm): control: 0.024±0.006, stimulation: 0.084±0.015, total stop time: control: 0.074±0.015s, stimulation: 0.25±0.062s, percentage of rewarded trials: control: 99.95±0.05%, stimulation: 97.95±1.09%). Compared to PV inactivation, however, this manipulation increased animals' early licks, both during the first 100 cm after run onset and beyond (Figures S5M and S5N). The animals' tendency to stop was no longer concentrated shortly after run onset (Figure S5O).

Note that we observed no effect in control sessions where optogenetics patch cables were only loosely mated with the implanted fiber optic cannulas (Figures S6M-S6Q). Since this manipulation affected PyrDown neurons as well as other neurons, we were not able to completely exclude the possibility that shutting down other neurons contributed to

the observed behavioral impairment. Nevertheless, these results suggest that activating PV neuronal firing as the animal approaches the reward zone, but not at the run onset, impairs the animal's behavior beyond the beginning of the trial.

Finally, since 15% of PyrDown neurons were tuned to reward (Figure S6G), we asked if bilateral PV activation around the reward zone impacts task performance. Using the same cohort of animals, we found this manipulation caused a similar but milder behavioral deficit than PV activation after 120 cm (Figures S5P-S5U). Thus, it appears PyrDown neurons may play a role in reward identification and reward prediction, and the shutdown of these neurons at run onset may allow for more precise reward prediction.

Discussion

Here, we discovered a circuit motif in the hippocampal CA1 region that responds to selected salient cues and signals the start of integration. This, in turn, allows for a more accurate prediction of the future reward.

Our results showed that animals can use relevant cues to initiate their counting of distance or time (referred to as "initiating cues"), and that the activity of the majority of CA1 pyramidal neurons aligns with such cues. We also discovered two subpopulations of pyramidal neurons, PyrUp and PyrDown, which exhibit either an increase or decrease in activity around the initiating cue. Of these two subpopulations, the PyrDown neurons are particularly engaged in initiating integration over distance or time. Our results suggest that PyrDown neurons, but not PyrUp neurons, are preferentially inhibited by parvalbumin-expressing (PV) basket cells. To determine the role of PV interneurons in controlling PyrDown neurons and starting integration, we performed optogenetic experiments, and demonstrated that: 1) reducing PV inhibition immediately after the initiating cue preferentially reduced the shutdown of PyrDown neurons and impaired the animals' ability to start integration correctly; 2) enhancing this inhibition at the same position had no significant impact on behavior; 3) enhancing PV inhibition before the reward zone abolished the gradual ramp-up activity of PyrDown neurons and impaired task performance.

Our results suggest that the shutdown of PyrDown neurons at the initiating cue primes them to gradually ramp up their activity towards the reward zone. This gradual ramp-up activity of the PyrDown neurons may provide a mechanism for representing integrated information on a slower time scale than neurons participating in IGSs. The inhibitory control exerted by PV interneurons over the PyrDown neurons can ensure a timely and correct start of subsequent integration.

Pyramidal neurons with and without IGFs may play different roles during information integration

CA1 pyramidal neurons with IGFs display a clear selectivity to specific distances or time points even without changes in external sensory inputs. Together, these neurons form an IGS, which can encode distance or time with a sub-second resolution(Mau et al., 2018;

Shimbo et al., 2021). IGFs and IGSs have been observed in animals performing various tasks, including memory tasks(Kraus et al., 2013; MacDonald et al., 2013, 2011; Pastalkova et al., 2008) and tasks with low memory demands(Salz et al., 2016; Shimbo et al., 2021; Villette et al., 2015). The percentage of pyramidal neurons participating in IGSs varies in these tasks, with a trend of fewer neurons involved in IGSs in tasks with low or no memory demands(Hirase et al., 1999; Pastalkova et al., 2008). Our active and immobile tasks, while lacking the explicit retrospective or prospective memory component, still require the animal to integrate over distance or time. In these tasks, there is a lower percentage of neurons participating in the IGSs than in tasks with higher memory demands. This is in line with the observation that fewer neurons display firing fields as rodents navigate through cue-poor environments under head-fixed conditions compared to cue-rich environments(Aghajan et al., 2015; Chen et al., 2018; Fischler-Ruiz et al., 2021).

That IGFs appear only in a subset of pyramidal neurons led us to question what role pyramidal neurons without IGFs play in supporting task performance. Our results suggest that a large proportion of pyramidal neurons without IGFs demonstrate significant tuning around the cue that signals the start of integration. These PyrUp and PyrDown neurons, lacking IGFs, typically display slower dynamics and are not tuned to specific distances or time points. However, these neurons still contain information about passage of time after the initiating cue (Figures S6A-S6E).

Based on these observations, we propose that pyramidal neurons with and without IGFs play distinct roles in memory encoding. They differ in terms of the spatial and temporal precisions of the information they encode. When higher memory demand or better encoding accuracy is required, more pyramidal neurons may express IGFs. These neurons with and without IGFs may thus complement each other in encoding ongoing experience.

CA1 PV interneurons are one of the circuit elements involved in starting integration

Our results suggest that PV interneurons play a role in enabling the animals to accurately initiate integration. However, these neurons are unlikely to be the only circuit elements engaged in the underlying computations.

First, our results demonstrate that PV interneurons preferentially inhibit PyrDown neurons while sparing PyrUp neurons, which also exhibit strong responses around the initiating cue. Additionally, our analysis indicates that PyrUp neurons contain information about the passage of time since the initiation cue (Figures S6D and S6E). Since previous research has suggested that PV basket cells tend to evoke weaker inhibition in CA1 pyramidal neurons located in the superficial part of the pyramidal layer(Lee et al., 2014), one might expect that PyrUp neurons are likely situated superficially within the layer. Yet, our data does not support this conclusion. An alternative explanation is that upstream regions, such as the CA3 and entorhinal cortex, may provide inputs with distinct patterns to PyrUp and PyrDown neurons around run onset. PyrUp neurons may receive stronger and more temporally synchronized excitation than PyrDown neurons, making them less susceptible to inhibition by PV basket cells(Royer et al., 2012).

Second, we observed that inactivating PV interneurons around run onset only weakly affects PyrUp neurons and pyramidal neurons with IGFs. These neurons may retain the information about distance or passage of time since the initiating cue, which may explain the mild effect of PV inactivation on behavior.

Third, we noticed that despite strongly shutting down pyramidal neurons, activating PV interneurons at run onset causes minor behavioral effects. One explanation for this is that the response of pyramidal neurons relies on the interaction between inputs from CA3 and entorhinal cortex within the dendrites. These inputs can carry information about distance or time since the start of integration(Brun et al., 2008; Davoudi and Foster, 2019; Robinson et al., 2017). PV activation transiently shuts down the somatic spiking of pyramidal neurons without substantially affecting their dendritic processing(Royer et al., 2012). As a result, the firing rate of pyramidal neurons returns to control levels shortly after the somatic inhibition is released (Figure 6B).

Together, our data suggest that the start of integration is likely encoded in diverse populations of neurons across various regions of the hippocampus. Here, we have identified one of the circuit motifs that involves the interaction between PV interneurons and PyrDown neurons.

The circuits initiating integration likely overlap with those delineating ongoing experience into discrete units

Our active task results reveal that run onset can serve as a salient cue to initiate IGSs and align the changes in neuronal activity in PyrUp and PyrDown neurons. This finding agrees with a previous report that IGSs can appear following the spontaneous onset of locomotion(Villette et al., 2015). Our results further demonstrate that the activity patterns of PyrUp and PyrDown neurons are specific to run onset at the beginning of a trial and do not occur around the spontaneous running onset in the middle of a trial. Additionally, both IGSs and PyrDown neurons' activity preferentially appear in tasks that require the animals to integrate over distance or time. Together, our data support that run onset may be a salient cue to start integration.

We also showed the initiating cue is not restricted to locomotion onset. In the immobile task, we speculate the last lick after the reward may serve as the initiating cue for integration over time. Previous studies have also shown that IGSs can occur after a sensory cue(Modi et al., 2014; Taxidis et al., 2020). These data suggest that animals can employ the salient sensory and motor cues in the trial structure to delineate continuous ongoing experience into individual trials.

Studies on human memory encoding have provided evidence that the continuous stream of experience can be segmented into discrete units through detecting event boundaries(Ben-Yakov and Henson, 2018; Zacks et al., 2010). However, the underlying neural circuits that perform the computation of segmenting ongoing experience into meaningful units and encoding sequential events remain largely unknown. The initiating cues described in our study may serve as event boundaries, and the process of integrating over distance or time within each trial in our tasks is likely comparable with integrating ongoing experience within a discrete unit.

The CA1 neural circuit motif we have identified, which responds to salient cues to start information integration over distance or time, may contribute to the computation performed in the process of detecting event boundaries and segmenting continuous experience into individual units.

Acknowledgments

We thank T. Harris, E. Moser, H. Inagaki, X. Zhao, A. Roxin, K. Citrin for comments on the manuscript; E. Pastalkova, L. Abbott, E. Schuman and D. Fitzpatrick for discussions; S. Sawtelle, B. Wisnicki and X. Zhao for help with the virtual reality setups. M. Klement, N. Daniel and machine shop at MPFI for making mechanical parts for the experimental setups; J. Wells and ARC at MPFI for taking care of animals. This work was funded by Max Planck Society and Max Planck Foundation, NIH R01 NS119503.

Author Contributions

Y.W. conceived the project. Y.W. and R.H. designed experiments (with input from D.P.). R.H. performed electrophysiological experiments. D.P., Y.W, and X.Z. performed behavioral experiments with optogenetics. Y.W. and R.H. analyzed data. Y.W. and R.H. wrote the manuscript, with contribution from all the authors.

Figure legends

Figure1. A simple behavioral task that expressed internally generated fields (IGFs)
A. Schematic of the virtual reality setup: The mouse is head-fixed, with the eyes aligned with the two monitors.
B. Task schematics for passive (top) and active (bottom) tasks.
C. Example speed traces (black) and licking activity (magenta) plotted against distance during three consecutive trials for mice performing the passive task (top) or active task (bottom). Reward: green. Start cue: gray.
D-E. Averaged speed traces (D) and Lick histograms (E) across mice trained in either the passive (3 animals, 8 recordings, in gray) or active task (4 animals, 10 recordings, in blue). Shaded area represents SEM (Same for other figures if not specifically stated).
F. Spike rasters of example pyramidal neurons recorded in the passive (left, no firing field) and active tasks (right, with a field).
G. Distribution of mean trial-by-trial activity correlations of all the pyramidal neurons recorded in the passive (536 neurons) and active tasks (7828 neurons).
H. The percentage of neurons with fields per recording in the passive (3 animals, 8 recordings) and active tasks (28 animals, 102 recordings). Each circle represents one recording.

Figure 2. Internally generated sequence (IGS) starts at run onset in the active task
A. Spike rasters plotted against distance showing the repeating trajectory of an IGS across 3 consecutive trials. Red lines denote transitions between two trials.
B. The same sequence as in Figure 2A averaged across the entire session, plotting the IGS over distance within the cue-constant segment.
C. Illustration of the sensory cues (including cue onset and reward) mice are exposed to across two consecutive trials.
D. Example speed traces and licking behavior plotted against time unfolded across 3 consecutive trials, illustrating the possibility that run onset instead of cue onset may serve as a salient cue to initiate IGSs. Run onsets: purple arrows.
E-F. Spiking activity of two example neurons (E), and an example IGS (F) from a single session, aligned to cue (left) vs. run onset (right).
G-H. Mean activity correlation (G) and spatial information (H) of neurons with IGFs when aligned to cue vs. run onset (650 neurons).
I. Mean trial-by-trial population correlation of IGSs using the same alignment methods.
J. The percentage of pyramidal neurons with IGFs per recording in the passive and active tasks after aligning to run onset.
K-N. Mean lick histogram binned by distance (reported p-value is for mean number of licks per bin between 30-100 cm) (K), mean running speed (L), total stop time from run onset to the trial's end (M), and mean activity correlation of neurons with IGFs (N), broken down by good (purple) and bad trials (gray).
O. An example IGS from the same session as in Figure 1F averaged across good (left) and bad (right) trials.

Figure 3. CA1 pyramidal neurons display distinct responses around the start of integration
A. After realigning to run onset, normalized firing rate profiles of all pyramidal neurons ordered by their firing rate ratio FR_{aft}/FR_{bef} (FR_{bef} = the averaged firing rate (FR) before run onset (-1.5->-0.5s), FR_{aft} = FR after run onset (0.5->1.5s), see gray bars on the top, 0s corresponds to run onset). Recordings with at least 15 good trials are included. PyrUp (2645 neurons) and PyrDown (1377 neurons) neurons are denoted by orange and purple boxes, respectively.
B. Firing rate profile averaged across all PyrUp neurons broken down into good and bad trials. Firing rate profile normalizing by its peak firing rate before averaging across neurons after yields similar results (Figure S2A).
C-D. Relative firing rate change before and after run onset (FRbef – FRaft)/(FRbef + FRaft) (C) and overall mean firing rate calculated between -1s and 4s (D) for PyrUp neurons.
E-G. Same as in Figures 3B-3D, for all recorded PyrDown neurons.
H. t-SNE embedding of firing rate profiles of all pyramidal neurons within -1.5 to 1.5 s round run onset. It shows a continuous cluster with PyrUp (orange) and PyrDown (purple) neurons grouped around the opposite ends of this cluster.
I-K. After realigning to spontaneous run onset (Spont. RO), the firing rate profile averaged across PyrUp neurons (dark blue) shows smaller changes than after aligning to trial start run onset (Trial RO, cyan) (I). Recordings with at least 15 spontaneous run bouts were included in the analysis. Relative firing rate change around run onset (J) and overall mean firing rate (K).
L-N. Same as in Figures 3I-3K, for PyrDown neurons.
O-P. Percentage of PyrUp (O) and PyrDown (P) neurons identified in the passive vs. active task.

Figure 4. CA1 parvalbumin-positive basket cells display sharp ramping activity around run onset
A-B. Spike waveform (A) and auto-correlogram (B) of a putative PV-basket cell. In (A), single waveforms are shown in gray and the averaged waveform is shown in black.
C. Raster plot showing spike theta phases (black dots) and firing rate as a function of time (orange) for the same cell as in Figures 4A and 4B.
D. Experimental design for optogenetic tagging experiments.
E. Interneurons plotted as a function of their mean theta phase and burst index. Each dot represents one interneuron. Color code corresponds to cluster identity from k-means clustering (Figure S3Q, see STAR methods). Green dots label neurons belonging to the putative PV-basket cell cluster. Overlaid crosses indicate interneurons identified as PV-positive from tagging experiments.
F. Normalized firing rate profiles of all the interneurons belonging to the putative PV-basket cell cluster, ordered by their firing rate ratio FR_{aft}/FR_{bef} around run onset (114 neurons). The green box denotes PV-Up neurons whose $FR_{aft}/FR_{bef} > 3/2$ (75/114 neurons).
G. Same as in Figure 3B, for PV-Up neurons.

H. Same as in Figure 4F, but for interneurons identified as PV-positive from the tagging experiments and at the same time belonging to the putative PV-basket cell cluster (13 neurons, 10/13 neurons with $FR_{aft}/FR_{bef} > 3/2$).
I. Same as in Figure 4G, but for PV-Up neurons within the tagged PV-basket cells. Bad trials are not shown because the number of bad trials is less than 15 trials in most of these recordings.
J-K. Relative firing rate change around run onset (J), and overall mean firing rate (K) for PV-Up neurons in Figure 4G, comparing good and bad trials.
O. Averaged and normalized firing rate profiles of PyrUp and PV-Up neurons (left), or PyrDown and PV-Up neurons (right). The peak of PV-Up neurons' activity is denoted by the gray bar (right).

Figure 5. Silencing PV-interneurons elevates the activity of PyrDown neurons and leads to behavioral impairment
A. Experimental setup for inactivating PV-interneurons. Light stimulation is applied with an optrode for 3 seconds starting after run onset of each trial.
B. Normalized firing rate profiles of all pyramidal neurons (335 neurons, 3 animals, 6 recordings) during control (left) and stimulation trials (right). Neurons are ordered by their firing rate ratio around run onset. PyrUp (129 neurons) and PyrDown (64 neurons) neurons are denoted by orange and purple boxes, respectively.
C. Normalized firing rate profile averaged across PyrUp neurons for control (orange) and stimulation trials (blue). Non-normalized firing rate profiles show similar results (Figure S4C).
D-F. Relative firing rate change around run onset (D), Mean firing rate before (E), and after run onset (F) for PyrUp neurons, comparing control and stimulation trials.
G-J. same as in Figures 5C-5F, for PyrDown neurons. Control (purple) and stimulation trials (blue).
K. Normalized firing rate profiles for pyramidal neurons with IGFs (49 neurons). PyrUp(Field) (31 neurons) and PyrDown(Field) (13 neurons).
L-O. Same as in Figures 5C-5F, for PyrUp neurons with IGFs.
P-S. Same as in Figures 5C-5F, for PyrDown neurons with IGFs.
T. Experimental setup to assess the behavioral effects of PV inactivation. The same stimulation protocol as in Figure 5A was applied to a different cohort of mice with optic fibers implanted bilaterally.
U. Histogram of licks binned by distance (10 mm per bin) for the first 100 cm for control (gray) and stimulation (blue) sessions (5 animals).
V-Y. Mean number of licks per bin calculated based on Figure 5U (V), the total stop time between run onset and the trial's end (W), mean running speed (X) and percentage of rewarded trials (Y) for control and stimulation sessions.

Figure 6. The ramp-up activity of PyrDown is necessary for task performance
A. Experimental setup for activating PV interneurons after run onset for 0.5s.

B. Normalized firing rate profile averaged across PyrUp neurons for control (orange) and stimulation trials (blue, 228 neurons, 5 mice, 14 recordings). Top: rank-sum test p-values for mean firing rate before (p_{bef}) and after (p_{aft}) run onset.
C. Mean firing rate between 0s and 1s after run onset.
D-E. Same as in Figures 6B and 6C, for PyrDown neurons (119 neurons).
F. Experimental setup to assess the behavioral effects of PV activation after run onset. Stimulation time was extended to 1.5s to enhance potential effects on behavior.
G-J. Same as in Figures 5U-5W, and 5Y, for PV activation after run onset.
K-T. Same as in Figures 6A-6J, for activating PV interneurons to remove the gradual ramp-up activity of PyDown neurons. Light stimulation was applied after the animal passed the 120cm mark in each stimulation trial. Figures 6M and 6O show the mean firing rate between 3s to 4s. PyrUp: 215 neurons, PyrDown: 108 neurons, 4 animals, 15 recordings.

Supplementary figure legends

Figure S1. Internally generated sequence (IGS) starts at run onset in the active task, related to Figures 1 and 2

A-D. The hippocampus-dependence of the active task is assessed by muscimol infusion experiments targeting CA1. (A) Mean lick histogram binned by distance during the control (gray) and muscimol (blue) sessions (9 animals, 10 recordings). (B) Mean number of licks per bin in the early portion of the trial. (C) Average speed curves binned by distance. (D) The percentage of trials where the animal received a reward.

E. Spiking activity of the two example neurons shown in Figure 2E, aligned to run onset (left column) vs. reward (right column).

F-G. Phase precession in neurons with IGFs. (F) A raster plot showing the theta phase change over time for the example pyramidal neuron in Figure 1F right that has an IGF and demonstrates phase precession. The spikes are aligned to run onset. (G) Pyramidal neurons with fields display significant phase precession relative to those without fields after aligning to run onset (7178 neurons). Phase precession is calculated as the difference between the oscillating frequency of individual neurons and local field potential theta oscillation frequency.

H-I. Alignment of all pyramidal neurons. (H) Mean activity correlation aligned to cue vs. run onset for all pyramidal neurons (7828 neurons). (I) Mean population correlation aligned to cue vs. run onset for all pyramidal neurons per recording (102 recordings).

J-K. Brain state is unchanged during the brief pauses before run onset. (J) Averaged multitaper spectrograms and theta/delta ratios aligned to the midpoints of long pauses, inter trial intervals (ITIs) 0-2s, or running bouts in one example recording. (K) Top: distribution of theta/delta ratios for different behavioral states pooled across recordings (13 animals, 25 recordings). Bottom: p-value matrix comparing theta delta ratios across brain states using pairwise Kruskal-Wallis tests.

L-N. Comparing behavioral parameters between good and bad trials. Mean number of licks per bin averaged between 30-100 cm (L), averaged speed traces (M), and percentage of rewarded trials in good and bad trials (N).

O. Left, firing rate profiles averaged across good trials for neurons with IGFs pooled across recordings in which there are at least 15 bad trials (145 neurons). Neurons ordered by time of peak firing rate relative to run onset. Right, the activity of the same sequence averaged across bad trials.

Figure S2. Pyramidal neurons display distinct responses around run onset, related to Figure 3

A. Normalized firing rate profile averaged across all PyrUp (left) and PyrDown (right) neurons broken down into good and bad trials. The results are similar to the non-normalized firing rate profile in Figures 3B and 3E.

B. Left, sequence formed by all pyramidal neurons with IGFs pooled across recordings, ordered by time of peak firing rate relative to run onset. Gray bars on the top indicate the temporal windows used to quantify the mean firing rate (FR) change around run onset

(FR_{bef} = FR before run onset (-1.5->-0.5s), FR_{aft} = FR after run onset (0.5->1.5s)). Recordings with at least 15 good trials are included. Right, same neurons as shown on the left, ordered by their firing rate ratio (FR_{aft}/FR_{bef}) around run onset. Orange and purple boxes denote the population of PyrUp(Field) and PyrDown(Field) neurons. The non-selected neurons are PyrOther(Field) neurons.

C. For each neuron shown in Figure S2A, log of firing rate ratio FR_{aft}/FR_{bef} is plotted as a function of its peak FR time. Each dot represents one neuron. Orange: PyrUp(Field) neurons ($FR_{aft}/FR_{bef} > 3/2$). Purple: PyrDown(Field) neurons ($FR_{aft}/FR_{bef} < 2/3$), Gray: other neurons.

D. Firing rate profile averaged across all PyrUp neurons with IGFs (431 neurons) broken down into good and bad trials (D1). Relative firing rate change around run onset (D2), and overall mean firing rate calculated between -1s and 4s (D3).

E. Same as in Figure S2D, for PyrDown neurons with IGFs (125 neurons).

F. Same as in Figure S2D, for PyrOther neurons with IGFs (92 neurons).

G. Same as in Figure S2D, for all PyrOther neurons (2998 neurons).

H. Depth distribution comparing all PyrDown and PyrOther neurons (left), PyrUp and PyrDown neurons (middle), and PyrUp and PyrOther neurons (right), respectively.

I. Normalized firing rate profile for PyrUp neurons identified by shuffling method (2943 neurons, see STAR methods) in good and bad trials (left). Relative firing rate change around run onset (middle) and overall mean firing rate (right).

J. Same as in Figure S2I, for PyrDown neurons identified by shuffling method (923 neurons).

K. Same as in Figure S2I, for PyrOther neurons identified by shuffling method (3154 neurons).

Figure S3. Pyramidal neurons display distinct responses around the start of integration, related to Figures 3 and 4

A-D. PyrUp and PyrDown responses are specific to run onset at the trial start in the active task. (A) After realigning to spontaneous run onset (Spont. RO), the firing rate profile averaged across PyrUp (left) and PyrDown (right) neurons (dark blue) shows smaller changes than after aligning to trial start run onset (Trial RO, cyan). Similar to Figures 3I and 3L, after selecting recordings with matching running speed between spontaneous runs and runs at the trial start (see STAR methods). (B) Percentage of pyramidal neurons whose FR_{aft}/FR_{bef} is significantly higher than the shuffled data after aligning to the spontaneous run onset (PyrUp-Spon, dark blue) is lower than the percentage after aligning to run onset at the trial start (cyan). (C) Percentage of pyramidal neurons whose FR_{aft}/FR_{bef} is significantly lower than the shuffled data after aligning to the spontaneous run onset (PyrDown-Spon, dark blue) is slightly but not significantly lower than the percentage after aligning to run onset at the trial start (cyan). (D) Firing rate profile averaged across PyrUp-Spon (left) or PyrDown-Spon (right) neurons after aligning to the spontaneous run onset (dark blue). The firing rate profile of the same subpopulation of neurons after realigning their activity to run onset at the trial start display smaller changes (cyan).

E-H. Percentage of PyrDown neurons is low in the passive task. (E-F) Averaged speed traces (E left), averaged speed (E right), lick histograms (F left) and mean number of licks per bin between 100-180 cm during the cue-constant segment (F right) across mice trained in either the passive task (3 animals, 8 recordings, in gray) or active task (4 animals, 10 recordings, in blue) after aligning to run onset. Recordings from the active task in which the running speed matches with the passive task are selected. (G-H) Percentage of PyrUp (G) and PyrDown (H) neurons identified in the passive task vs. in the active task. Recordings with matching speed are selected, as in Figure S3E.
I-O. PyrUp and PyrDown responses in an immobile task. (I) Task schematic for the immobile task. (J) IGS is present after aligning the neuronal activity to the last lick of the previous trial (53/748 neurons). (K) Normalized firing rate profiles of all pyramidal neurons ordered by their firing rate ratio FR_{aft}/FR_{bef} (FR_{bef} = the mean firing rate (FR) before last lick (-1.5->-0.5s), FR_{aft} = FR after last lick (0.5->1.5s), 0s corresponds to the last lick) within each subpopulation (PyrUp, PyrOther and PyrDown). PyrUp (377 neurons) and PyrDown (199 neurons) neurons identified by shuffling method are separated by orange and purple lines, respectively. (L) Normalized firing rate profile averaged across all PyrUp neurons into good trials. (M) Same as in Figure S3L, for PyrDown neurons. (N) The percentage of PyrUp neurons identified in the immobile task (dark blue) is higher than that identified in the active task (cyan). (O) Same as in Figure S3N, for PyrDown neurons.
P. Confocal images of CA1 from a PV-Cre x Ai14 mouse. From left to right, tdTomato expression, PV immunostaining (GFP), and overlaid images. Arrows point to cells that are co-labeled for tdTomato and GFP.
Q-V. Results from the optogenetic tagging experiments. (Q) A three-dimensional view of the 6 interneuron clusters in the PCA space. (R) Normalized firing rate profiles of the interneurons that are PV-positive from the tagging experiments but do not belong to the putative PV-basket cell cluster. (S-V) Comparisons of tagged PV-basket cells and putative PV-basket cells. (S) Auto-correlograms (ACGs) of cells belonging to the putative PV-basket cell cluster. On the top shows the mean+/- sem of the ACG peak time averaged across all cells. (T) Same as in Figure S3S, for tagged PV-basket cells. (U) Theta phase histograms of cells belonging to the putative PV-basket cell cluster. On the top shows the mean+/- sem of the peak theta phase averaged across all cells. (V) Same as in Figure S3U, for tagged PV-basket cells.

Figure S4. PV interneurons preferentially inhibit PyrDown neurons, related to Figure 5
A-E. Optrode-mediated inactivation of PV interneuron activity at run onset. (A) From Figure 5A, experimental setup. (B) Example putative basket cells, one is effectively inactivated by light (left), while the other is not affected (right). (C) Firing rate profile averaged across PyrUp (left) or PyrDown (right) neurons for control (orange) and stimulation trials (blue). (D) Number of PyrUp neurons with IGFs identified in the control and stimulation trials (left). Mean activity correlation of PyrUp neurons with IGFs during the control trials vs. mean activity cross-correlation between control and stimulation trials (right). (E) Same as in Figure S4D, but for PyrDown neurons.
F-J. Bilateral optogenetic inactivation of PV interneurons at run onset. (F) From Figure 5T, experimental setup. (G) The percentage of trials where the animal paused between

run onset and the trial's end, comparing control and stimulation sessions. (H-J) Mean number of licks per bin from 100-140cm (H), 140-180cm (I), and after 180cm (J).
K-O. Optrode-mediated inactivation of PV interneurons at reward delivery. (N) Experimental setup. Light stimulation is applied using an optrode for 3 seconds starting at the reward onset to cover run onset of the following trial. (L) Firing rate profiles of all the pyramidal neurons (939 neurons, 5 animals, 17 recordings) during control (left) and stimulation trials (right). Neurons are ordered by their firing rate ratio around run onset. PyrUp (368 neurons) and PyrDown (173 neurons) neurons are denoted by orange and purple boxes, respectively. (M) Normalized firing rate profile averaged across PyrUp neurons (left) for control (orange) and stimulation trials (blue), and PyrDown neurons (right) for control (purple) and stimulation trials (blue). Top: rank-sum test p-values for mean firing rate before (p_{bef}) and after (P_{aft}) run onset, and relative firing rate change around run onset ($p_{frchange}$). (N-O) Same as in Figures S4L and S4M, but for PyrUp and PyrDown neurons with IGFs.
P-U. Bilateral optogenetic inactivation of PV interneurons at reward delivery. (P) Experimental setup. The same stimulation protocol as in Figure S4K was applied to the same cohort of mice shown in Figure 5T. (Q) Histogram of licks binned by distance for the first 100 cm in control (gray) and stimulation (blue) sessions (5 animals). (R-T) The total stop time between run onset and the trial's end (R), mean running speed (S), and percentage of rewarded trials (T). (U) The averaged percentage of time the animal stopped between 0-100 cm after run onset in each trial. In this case, the stop time between 0 and 150 cm is used in the denominator as the total stop time to avoid the increase in slow running induced stop time as the animal approaches the reward.

Figure S5. The ramp-up activity of PyrDown is necessary for task performance, Related to Figure 6
A-E. Firing rate change of PyrUp and PyrDown neurons with IGFs during running onset PV activation. (A) As in Figure 6A, experimental setup. (B) Left, normalized firing rate profile averaged across PyrUp neurons with IGFs in control and stimulation trials (left, 49 neurons). Right, mean firing rate 0-1 seconds after run onset. (C-E) Same as Figure S5B, for PyrDown neurons with IGFs (C), PyrOther neurons (D), and PyrOther neurons with IGFs (E), respectively.
F-J. Firing rate change of PyrUp and PyrDown neurons with IGFs during PV activation in later portion of a trial. (F) As in Figure 6K, experimental setup to activate PV interneurons after the animal passed the 120cm mark in each stimulation trial. (G-J) Same as Figures S5B-S5E, for stimulation after the 120cm mark. The right column plot in each figure shows mean firing rate 3-4 seconds after run onset in stimulation and control trials.
K-L. Bilateral optogenetic activation of PV interneurons at run onset. (K) From Figure 6F, experimental setup. (L) Mean running speed for control and stimulation sessions.
(M-O) Bilateral optogenetic activation of PV interneurons after the 120m mark. (M) As in Figure 6P, experimental setup to assess the behavioral effects of removing the ramp-up activity of PyDown neurons. The mean number of licks per bin between 100-140cm (N) and the percentage of time stopped between 0-100cm (O) for control and stimulation sessions.

P-U. Bilateral optogenetic activation of PV interneurons at reward zone. (P) Experimental setup. (Q) Histogram of licks binned by distance in the first 100cm of the trial for control and stimulation sessions. Reported p-value is for mean number of licks in this same period. The total stop time between run onset and the trial's end (R), percentage of rewarded trials (S), mean running speed (T), the percentage of time stopped between 0-100cm (U).

Figure S6. The ramp-up activity of PyrDown might encode reward and reward prediction, related to Figures 5 and 6

A-C. Bayesian decoding using PyrDown neurons without IGFs. (A) Decoding results of a single recording session. Color bar indicates posterior probabilities. Blue line denotes decoder's most confident estimation. (B) Decoding results averaged across all recording session (19 animals, 29 recordings). (C) Decoding loss determined using tenfold cross validation compared with the loss of the shuffled data.

D-E. Bayesian decoding using PyrUp neurons without IGFs. (D) Decoding results averaged across all recording session (23 animals, 77 recordings). (E) Decoding loss determined using tenfold cross validation compared with the loss of the shuffled data.

F-G. Peak detection for PyrUp and PyrDown neurons. (F) From left to right: example raster plots of pyramidal neurons with significant peaks at run onset (Run), the first lick of each trial (Lick), and reward delivery (Rew), respectively. Red lines are the firing rate profile, and grey area represents the range between the 1st and 99th percentile of shuffled data. Black bars show the location and span of detected peaks. (G) Percentage of PyrUp (left) and PyrDown (right) neurons belonging to each of the following categories: No Peak, Run, Lick, and Rew Peaks. If a neuron belongs to more than one categories simultaneously, it is grouped into the category where the firing rate displays the highest change after alignment.

H-L. Optogenetic inactivation control experiments. (H) Experimental design. Light delivery protocols are identical to previous experiments, but the patch cables were adjusted not to be in contact with the implanted fiber optic cannulas, precluding light delivery into the brain. (I) Histogram of licks binned by distance in the first 100cm of a trial for control and stimulation sessions. Reported p-value is for mean number of licks in this same period. The total stop time between run onset and the trial's end (J), mean running speed (K), and percentage of rewarded trials (L).

M-Q. Optogenetic activation control experiments. (M) Experimental design. Following the same procedure as in Figure S6H. (N-Q) Same as in Figures S6I-S6L, but for optogenetic activation.

Methods

Mice

This study was based on both male and female mice (age > 8 weeks). Male mice were used in the running tasks because they were found to exhibit more consistent running behavior. We used three mouse lines: C57Bl/6J (JAX #000664), PV-IRES-Cre (JAX #017320) (Hippenmeyer et al., 2005), and Ai14 (JAX # 007914) (Madisen et al., 2012). All procedures were in accordance with protocols approved by the Institutional Animal Care and Use Committee at Max Planck Florida Institute for Neuroscience. Mice were housed in a 12:12 reverse light: dark cycle and behaviorally tested during the dark phase.

Virtual reality setups

For the virtual reality (VR) setups, a small treadmill (Janelia Design) was positioned in front of two visual displays, such that after head-fixation, the eyes aligned with the two visual displays. Customized software was written using Psychtoolbox to display the virtual environment. An Arduino control board was used to control when to display the visual stimuli. For the small treadmill, the animal's speed was measured using an encoder attached to the back wheel axis. A microprocessor-based (Arduino) behavioral control system (the miniBCS board, designed at Janelia) interfaced with a MATLAB graphical user interface controlled the trial structure, the water valve, and the encoder. A separate lick port detector (designed at Janelia) was used to convert a touch on a metal lick port into a digital pulse and to send the information to the miniBCS board. In another version of the VR setups, instead of using two monitors, a curved screen was used where the virtual reality environment was projected onto the curved screen using a projector (AKASO Mini Projector, a design kindly shared by Christopher Harvey's lab at Harvard University). In this case, customized software written with Unity was used to display the virtual environment.

In addition, a separate microprocessor (Arduino) interfaced with a customized MATLAB graphical user interface was used to operate the laser or laser diode on-off for the optogenetic perturbation experiments and to control the closed-loop manipulation of PV interneurons. Behavioral data were monitored and recorded as well using MATLAB functions.

Behavioral training

Before any surgery was performed, running wheels were added to the home cages. At 3–5 days after the headbar or fiber implantation, mice were placed on water restriction (typically 0.8-1 ml per day). After each training or recording session, mice were supplemented with additional water to ensure the amount of water intake per day. After habituating the animals to the treadmill for at least 1-2 days, animals were trained to run head-fixed on the treadmill.

In the passive task, each trial started with a gray-colored visual cue. The animal was required to run for 180 cm while this visual stimulus stayed constant, then a water reward was automatically delivered to signal the end of the trial. After that, the next trial started at least after 0.5 s and until the animal's speed has exceeded 30 cm/s for more than 0.3s and the time since the last lick has exceeded 0.3 seconds. Therefore, there was a random delay of at least 0.5 s until the next trial started. It took about 1-2 weeks for the animals to run smoothly on a treadmill and to perform this task.

In the active task, a trial started with a visual grating stimulus, the stimulus was either 0.5 sec or 1 sec long, and stayed the same within each session. After that, a gray-colored stimulus turned on. The animal was required to run for a fixed distance (180 cm) while this visual stimulus stayed constant, then it must lick within a 40 cm (in some sessions, it is 80 cm) reward zone to receive a water reward. If licking triggered a reward, the screens turned black for either 0.5 second or 1 second (kept constant within each session); otherwise, they turned black to signify the error. It took about 2 weeks for the animals to learn this task.

In the immobile task, the animal sat within a plastic tube(Guo et al., 2014). Each trial started with a 1 sec visual grating stimulus, which was then followed by a gray-colored stimulus that lasted 4 second. After that, there was a reward zone lasting 2 second. If the animal licked within the reward zone, a drop of water reward was triggered, and the screens turned black for a random time between 0.5-2.5 second. If the animal failed to lick within the reward zone, the screens turned black for a random time between 0.5-2.5 second. To train the animal to perform this task, the animal was first habituated to stay in the tube, and then gradually applied head-fixation. This task took about 2 weeks to train.

Virus injection, headbar, cannula and fiber implantation

Adult mice (2-4 months of age) underwent aseptic stereotaxic surgery to implant a custom lightweight 3D printed headplate under isoflurane anesthesia (2-3% for induction, 1%–1.5% for maintenance). buprenorphine SR LAB (0.5 mg/kg, SC) or buprenorphine (0.1 mg/kg, SC), and Meloxicam SR (5 mg/kg, SC) was administered immediately after the surgery. For acute extracellular recordings, after training to perform behavior tasks, craniotomies were performed which were centered around antero-posterior 2.1 mm from bregma, mediolateral +/-1.7 mm from the midline to target dorsal CA1 region. Meanwhile, a ground wire was attached to the headbar, and a thin layer of silver paint (GC ELECTRONICS 22-0023-0000) was applied to the surface of the headbar for noise reduction during the recording. The skull was covered using KwikSil (World Precision Instruments) and was only removed during recordings.

For extracellular recordings with optogenetic manipulation of PV interneurons, AAV1_hSyn1-SIO-stGtACR2-FusionRed (Addgene 105677, 2.1e+12 after 10 fold dilution) was used for optogenetic inactivation, and AAV5-Ef1a-double-floxed-hChR2(H134R)-mCherry-WPRE-hGHpA (Addgene 20297, titer 1.4e+13) was used for optogenetic activation. 50 nl virus per hemisphere was injected bilaterally in the CA1 of PV-IRES-Cre mice at least 3 days before the headbar implantation, and at least 3 weeks before the recording. The following coordinates were used for viral injections: 2.1 mm from bregma, mediolateral +/-1.7 mm from the midline and 1.24 mm dorsoventral from the brain surface.

The injection system comprised a pulled glass pipette (broken and bevelled to 15-20 μm inside diameter; Drummond, 3-000-203-G/X), backfilled with mineral oil (Sigma). A fitted plunger was inserted into the pipette and advanced to displace the contents using a manipulator (Drummond, Nanoject II or Nanoject III). Retraction of the plunger was used to load the pipette with the virus. The injection pipette was positioned onto a Kopf manipulator.

For optogenetic experiments without extracellular recordings, the viral injection procedure was the same as described in the last paragraph. At least 3 days after the viral injection, optical fibers (core diameter of 200 um) were chronically implanted bilaterally to target the CA1 region bilaterally using the following coordinates: 2.1 mm from bregma, mediolateral +/-1.7 mm from the midline and 0.9 mm dorsoventral from the brain surface.

For muscimol infusion experiments, guide cannulas (26 Gauge) were implanted bilaterally above the CA1 region (coordinates: 2.1 mm from bregma, mediolateral ±1.7 mm from the midline and 1.1 mm dorsoventral from the brain surface) during the head bar surgery. A dummy cannulas (33 Gauge) of the same length as the guide cannulas were inserted to the guide cannulas.

Optogenetics without extracellular recordings

For each optogenetic session, a control session (~40 trials) was performed. It was then followed by a stimulation session (~100 trials in total), where the photostimulation was deployed every third trial. After that, there was a post stimulation control session (~40 trials). To prevent mice from distinguishing photostimulation trials from control trials through stimulation light, a masking blue light (470 nm LEDs (Thorlab)) was on throughout the sessions. For both stGtACR2 and ChR2, we used a 473 nm laser (Ningbo Lasever Inc.). The laser power used was <= 5 mW. During the stimulation, 100 Hz light pulses were used to reduce the heating effect of a constant laser light. The duty cycle was varied to adjust the light power.

For PV inactivation using stGtACR2, the stimulation lasted 3 seconds. The stimulation can be triggered at (1) the reward delivery, (2) the running onset or (3) at 120 cm location during the cue-constant segment. The run onset stimulation is triggered at the first time point where the animals speed exceeded 10 cm/s for at least 200 msec after the trial start. The stimulation trial types were randomly selected for each stimulation session. The behavior analysis was performed using all the trials during the stimulation session. Only considering the stimulated trials led to similar results.

For PV activation using ChR2, the stimulation lasted 1.5 seconds.

Acute extracellular electrophysiology

Two days before the recording, the animal was acclimated to the recording condition: including turning on the microscope light, removing Kwiksil that covered the skull, and adding saline to keep the craniotomy wet. On the day before the recording, craniotomy was opened. During electrophysiological recordings, a 64 channel silicon probe (neuronexus, buzsaki64sp) was slowly lowered into the hippocampal CA1 region. Data

from all channels were filtered (0.3 Hz to 10 kHz), amplified (gain = 400) and continuously sampled at 20 kHz using the Amplipex system (16-bit resolution)(Berényi et al., 2014). Time stamps of behavioral events, and electrophysiological recording data were synchronized, recorded and stored on a computer.

For extracellular recordings with optogenetics, a 64 channel silicon probe with fibers mounted on the shanks (neuronexus, buzsaki64sp-OA64LP) was used. Photostimulation followed the same protocol as described in the optogenetics section above, except that for PV activation, the stimulation lasted 0.5 second. The light source was a self-constructed laser diode array (6 diodes, 450 nm, osram-os, PL450B). Each diode was coupled to one shank on the probe. Typically, 2-3 diodes were coactivated during the stimulation. The stimulation laser power was < 1.2 mW at the tip of the probe.

Following recordings with PV activation, PV-positive interneurons were tagged using 1ms pulses of blue light. Spike times around each pulse were binned with a resolution of 1ms and the significance of light responses in a 5ms window after the light pulse was assessed using the stimulus-associated spike latency test (SALT)(Kvitsiani et al., 2013). Neurons with a $P < 0.01$ that responded to at least 40% of light pulses were identified as PV-positive. 30-40 tagging pulses were applied per recording.

Muscimol infusion

Muscimol hydrobromide (Tocris-0289) was dissolved in 0.9% saline. The control solution was saline. The Muscimol injections were carried out as follows. First, an injection cannula was connected to a 10-µl Hamilton syringe through Tygon tubing (Tygon 720993) and filled with muscimol (1 mg ml^{-1}) or saline (0.9%). Then the syringe was mounted into a microinjection pump (UMP3 with SYS-Micro4 controller). At the beginning of the injection procedure, the dummy cannula was removed from the guide cannula and replaced by the injection cannula (33 Gauge) which extended 0.5 mm deeper into the brain than the guide and dummy cannulae. Then 300-500 nl muscimol or saline were slowly injected (100 nl/min) into CA1 and the injection cannula was left in place for another 3 min after the infusion was complete. Next, the dummy cannula after cleaned with alcohol and dipped in sterile mineral oil was inserted back into the guide cannula. During the infusion, animals were performing the active task with water automatically delivered at the end of each trial. Animals did not show signs of stress or discomfort during the procedure. The animals were released from the setup after the infusion, and ~30 min after the completion of infusion, animals were placed back onto the VR setup. A typical muscimol infusion recording was composed of one control session before the infusion, and multiple recording sessions at 30 min, 1 hour, 2 hours after the infusion.

Spike sorting

To identify spikes, we performed off-line spike sorting on the recorded files following published methods using Klusters(Hazan et al., 2006) and Kilosort(Pachitariu et al., 2016). Units were further selected based on the percentage of spikes that violated refractory period and the mahalanobis distance of the unit from other units.

Histology

Mice were perfused transcardially with PBS followed by 4% PFA. Brains were post fixed overnight and transferred to PBS before sectioning using a vibratome. Coronal 50 µm free-floating sections were processed using standard fluorescent immunohistochemical techniques. PV immunoreactivity (Swant, GP72; 1:2000, guinea pig). The primary antibody was visualized by Alexa Fluor 488 AffiniPure Donkey Anti-Guinea Pig IgG (H+L) (1:1,000, Jackson ImmunoResearch Laboratories, 706-545-148).

Behavior analysis

To calculate how the speed changed over distance during the cue-constant segment, the histogram of speed within each trial was calculated using 1 mm distance bins. 15 trials were randomly selected from each session, and the average and SEM of speed were calculated across all the selected trials from all the sessions in each task. Similarly, to calculate how the number of licks changed over distance, a lick histogram with a bin size of 1 cm was first calculated for each trial. Then the same calculation as the speed was applied to get the average and SEM. To calculate the overall mean speed or lick within a certain distance range, the mean speed or lick number is first calculated for each session, then averaged across sessions from the same task. To calculate total stop time, we first smoothed running speed using moving average with an 80 ms window, and then summed the time when the speed was lower than 1 cm/s from the running onset to the end of the trial.

To find recordings with matching running speed between the passive and active tasks, we selected animals that were trained on the active task around the time similar to those trained on the passive task. As a result, we were able to identify 4 animals (10 recordings in total) where the mean speed did not differ from the passive task recordings.

Extracellular recording analysis

Alignment to sensory or motor cues

For both the passive and active tasks, both the neuronal activity and the behavior of each trial were aligned to either the start cue onset or to the running onset. The running onset for each trial was defined as the onset of the first running bout that lasted more than 0.3 sec with a speed > 10cm/s, starting from the previous trial after the animal had travelled 180 cm cue-constant segment. The onset was when the running speed reached 1 cm/s before the running bout and after 180 cm in the cue-constant segment of the previous trial. If the speed never reached 1 cm/s, the time point when the speed was the lowest was considered as the onset, and this trial was classified as “no clear run onset”.

Firing rate profile of each neuron

Pyramidal neurons were identified based on their spike waveforms, and their firing rates fell between [0.15 7] Hz. The spike train of each pyramidal neuron was first smoothed with a Gaussian function (s.d. = 30 ms) and then averaged across trials to get the

averaged firing rate profile of that neuron. When examining how the firing rate changes over distance, the spike train was first binned using 1 mm spatial bins, and then smoothed with a Gaussian function (s.d. = 20mm). Normalized firing rate profile of PyrUp or PyrDown neurons was calculated by first normalizing the firing rate profile of each neuron by its max firing rate and then averaged across the selected population.

Firing field identification

The averaged firing rate profile of each neuron was used to identify firing fields (internally generated fields). To identify firing fields over distance, the following criteria were applied: 1) a minimum mean firing rate of 0.09 Hz; 2) minimum mean trial-by-trial spearman correlation of the firing rate profile > 0.15 and minimum spatial information(Markus et al., 1994) > 0.25 bits/s; or minimum mean trial by trial correlation > 0.09 and minimum spatial information > 0.7 bits/s. 3) total number of trials > 15, and the neuron was active in at least 40% of the trials. 4) the maximum field width was 150 cm, measured by the width when the firing rate fell below 10% on both sides of the peak firing rate. 5) there was no other peak within 30 cm outside the field. The parameters were chosen based on visual inspection.

To identify firing fields over time, we used similar criteria as mentioned above. Some of the parameters were readjusted based on visual inspection: minimum mean trial by trial correlation > 0.12 and minimum spatial information > 1 bits/s; or minimum mean trial by trial correlation > 0.09 and minimum spatial information > 2.5 bits/s. The maximum field width was set to 4.5 sec. There was no other peak within 1.7 sec outside the field. For the immobile task, the same method was used to identify firing fields over time. The difference was that the neuronal activity was aligned to the last lick of each trial in the immobile task, and the following parameters were used: minimum mean trial by trial correlation > 0.1 and the minimum spatial information > 0.65 bits/s.

Auto-correlogram

Spike time auto-correlogram of each neuron was calculated after binning its spike train using 1 ms time bins.

Phase precession

Phase precession was calculated as the difference between the theta modulation frequency of individual neurons and the theta frequency of the local field potential (LFP). The theta modulation frequency of individual neurons was calculated using the peak time of its auto-correlogram within 100-200 ms and -100- -200 ms windows(Chrobak and Buzsáki, 1998). One LFP trace recorded from the CA1 pyramidal layer was filtered with a third order Chebyshev Type II filter (4-16 Hz). LFP instantaneous frequency in the theta band was calculated using Hilbert transform. The instantaneous frequency was then averaged over each trial and across trials to compute the LFP theta frequency.

Criteria for good and bad trials

For the active task, a good trial was defined as 1) the animal stopped for less than 2 s after the running onset, 2) it stopped at the reward location, and 3) it received reward. Otherwise, the trial was considered a bad trial.

For the immobile task, trials where mice did not lick in the reward zone or began licking before the halfway point of the delay period were labeled as bad trials.

Identification of PyrUp and PyrDown neurons

The change in firing rate around the run onset for each neuron was defined as the ratio between the averaged firing rate in a window 0.5 to 1.5 seconds (FRaft) and -1.5 to -0.5 seconds (FRbef) about the running onset (FRaft/FRbef). The PyrUp neurons were neurons whose FRaft/FRbef > 3/2, while the PyrDown neurons were neurons whose FRaft/FRbef < 2/3. PyrOther neuron were neurons whose FRaft/FRbef were between 3/2 and 2/3. The relative firing rate change of the average firing rate profile around run bouts and trial run onsets were calculated for each neuron in a window 0.5 to 1.5 and -1.5 to -0.5 seconds about the running onset with the formula (FRbef – FRaft)/(FRbef + FRaft).

The same criteria are used to identify PV-Up neurons.

To avoid bias in grouping neurons, an additional shuffling method was used to identify PyrUp and PyrDown neurons. Shuffled distributions of FRaft/FRbef were created by performing randomized circular shifts to the firing rate profile of each trial and recalculating FRaft/FRbef 1000 times. Neurons with a firing rate change that was above the 95th percentile or below the 5th percentile of the shuffled distribution were labeled as a PyrUp or PyrDown neuron, respectively.

The same method was used to identify PyrUp and PyrDown neurons with respect to the run onset in the passive task.

PyrUp and PyrDown neurons with respect to running bouts in the active task

Run bouts were identified as periods where locomotion exceeded 10cm/s for a duration of at least 0.5 seconds. The onset of each run bout was traced back to the point where speed first exceeded 2 cm/s. If running speed in the window 0.5 seconds before a run bout exceeded 10cm/s at any time point that run bout was excluded from analysis. Run bouts that occurred within the first 50 cm of a trial were also excluded from the analysis. Spike times for each neuron were aligned to the run bouts and firing rates were calculated in 2.5 millisecond bins and convolved with a Gaussian filter with a standard deviation of 30 milliseconds. PyrUp and PyrDown neurons were identified for run bouts using the same shuffling method as before. Recordings with fewer than 15 run bouts were excluded from analysis.

Speed matching was performed for each recording by first calculating the mean speed and standard deviation of running bouts in a period from -1.5 to 0s and 0 to 1.5s around bout onsets. Trial run onsets that fell within one standard deviation of the mean speed for both periods were included for analysis. Recordings with less than 15 total run bouts and less than 15 speed-matched trial run onsets were excluded from analysis. Recordings with at least 15 spontaneous run bouts were included in this analysis.

t-SNE

The t-distributed stochastic neighbor embedding (t-SNE) method(Maaten and Hinton, 2008) was applied to the normalized firing rate profile (normalized to the neuron's peak firing rate) of all the pyramidal neurons in the window between -1.5 and 1.5 seconds around the running onset.

Theta phase

The peaks, valleys and zero crossing points of LFP were detected and assigned as phase 0, 180 and 90 or 270, respectively. Phases between these points were linearly interpolated(Belluscio et al., 2012). Peaks in the LFP corresponded to the minimum firing of CA1 pyramidal cells. Please refer to Wang et.al. 2015(Wang et al., 2015) for more details. Theta phase histogram of each neuron is calculated using 5 degree bins between 0 and 360 degree.

Interneuron clustering

Interneurons were identified based on their spike waveforms and their auto--correlograms. Principle component analysis (PCA) was performed on the matrix formed by the normalized theta phase histograms of all the interneurons. The number of PCA components was selected such that the accumulated explained variance reached 95% unless the number of components was larger than 30. The same treatment was done on the matrix formed by the auto-correlograms of all the interneurons. The PCA components of the theta phase histograms, the auto-correlograms, and the estimation of the depth of interneurons relative to the center of the pyramidal layer were features used to perform kmean clustering of interneurons. The number of clusters was determined by the evalclusters function in matlab, and then went through visual inspection. The putative PV basket cell cluster was identified based on similarities with well-established firing phenotypes of this cell group(Klausberger and Somogyi, 2008; Royer et al., 2012). The estimation of depths of interneurons and pyramidal neurons relative to the center of the pyramidal layer was calculated following the method in Mizuseki et.al., 2011(Mizuseki et al., 2011).

Decoding analysis

For each recording session, we trained a naïve Bayesian classifier built around the Matlab function fitcnb(Mau et al., 2018) with population activity of all the PyrDown neurons without firing fields. Recordings with at least 25 good trials and 15 PyrDown neurons are included in the analysis. The PyrDown neurons were detected by thresholding FRaft/FRbef. Bayesian decoding loss was determined using tenfold cross validation. Chance was calculated by calculating the loss after performing randomized circular shifts of the firing rate profiles to each trial for N = 50 times. The time bin for decoding was 0.2 second.

Spectrograms and brain state changes

Multitaper spectrograms were constructed from the LFP channels in the layer center of CA1 using the mtspecgramc function in the Chronux library (http://chronux.org/). A sliding window of T = 1s and a frequency resolution of Δf = 2 Hz was used. The time-half-bandwidth product and the number of tapers used were calculated as in Prerau et.al. 2017(Prerau et al., 2017). Brain state was defined by a theta/delta ratio, calculated as the quotient of the average power in the 6-8 Hz and 2-4 Hz bands.

Long pauses and inter-trial intervals

Long pauses were defined by immobile periods when running speeds were below 2cm/s for 5s or longer. Running bouts were defined by periods when running speeds were 10cm/s or greater for a minimum of 3s. Inter-trial intervals were defined as the periods in

between the delivery of the sucrose reward in one trial and the running onset of the following trial. Slow runs were defined as periods where running speeds fell between 5 and 20 cm/s.

Peak detection

Average firing rate curves aligned to the onset of running, predictive licking, or reward delivery were obtained for each neuron. Null distributions were created by shuffling firing rate curves and averaging across n = 1000 shuffles. A neuron was defined as having a peak relative to a particular behavioral stimulus if its firing rate exceeded the 99th percentile of the null distribution for a period of at least 0.1s within -1 to 1 s window around the stimulus.

References

Aghajan, Z.M., Acharya, L., Moore, J.J., Cushman, J.D., Vuong, C., Mehta, M.R., 2015. Impaired spatial selectivity and intact phase precession in two-dimensional virtual reality. Nat. Neurosci. 18, 121–128. https://doi.org/10.1038/nn.3884

Belluscio, M.A., Mizuseki, K., Schmidt, R., Kempter, R., Buzsaki, G., 2012. Cross-Frequency Phase-Phase Coupling between Theta and Gamma Oscillations in the Hippocampus. J. Neurosci. 32, 423–435. https://doi.org/10.1523/JNEUROSCI.4122-11.2012

Ben-Yakov, A., Henson, R.N. (Eds.), 2018. The Hippocampal Film Editor: Sensitivity and Specificity to Event Boundaries in Continuous Experience. J. Neurosci. 38, 10057–10068. https://doi.org/10.1523/JNEUROSCI.0524-18.2018

Berényi, A., Somogyvári, Z., Nagy, A.J., Roux, L., Long, J.D., Fujisawa, S., Stark, E., Leonardo, A., Harris, T.D., Buzsáki, G., 2014. Large-scale, high-density (up to 512 channels) recording of local circuits in behaving animals. J. Neurophysiol. 111, 1132–1149. https://doi.org/10.1152/jn.00785.2013

Brun, V.H., Leutgeb, S., Wu, H.-Q., Schwarcz, R., Witter, M.P., Moser, E.I., Moser, M.-B., 2008. Impaired Spatial Representation in CA1 after Lesion of Direct Input from Entorhinal Cortex. Neuron 57, 290–302. https://doi.org/10.1016/j.neuron.2007.11.034

Cembrowski, M.S., Bachman, J.L., Wang, L., Sugino, K., Shields, B.C., Spruston, N., 2016. Spatial Gene-Expression Gradients Underlie Prominent Heterogeneity of CA1 Pyramidal Neurons. Neuron 89, 351–368. https://doi.org/10.1016/j.neuron.2015.12.013

Chen, G., King, J.A., Lu, Y., Cacucci, F., Burgess, N., 2018. Spatial cell firing during virtual navigation of open arenas by head-restrained mice. eLife 7, e34789. https://doi.org/10.7554/eLife.34789

Chrobak, J.J., Buzsáki, G., 1998. Gamma Oscillations in the Entorhinal Cortex of the Freely Behaving Rat. J. Neurosci. 18, 388–398. https://doi.org/10.1523/JNEUROSCI.18-01-00388.1998

Danielson, N.B., Zaremba, J.D., Kaifosh, P., Bowler, J., Ladow, M., Losonczy, A., 2016. Sublayer-Specific Coding Dynamics during Spatial Navigation and Learning in Hippocampal Area CA1. Neuron 91, 652–665. https://doi.org/10.1016/j.neuron.2016.06.020

Davoudi, H., Foster, D.J., 2019. Acute silencing of hippocampal CA3 reveals a dominant role in place field responses. Nat. Neurosci. 22, 337–342. https://doi.org/10.1038/s41593-018-0321-z

Fischler-Ruiz, W., Clark, D.G., Joshi, N.R., Devi-Chou, V., Kitch, L., Schnitzer, M., Abbott, L.F., Axel, R., 2021. Olfactory landmarks and path integration converge to form a cognitive spatial map. Neuron 109, 4036-4049.e5. https://doi.org/10.1016/j.neuron.2021.09.055

Freund, T.F., Katona, I., 2007. Perisomatic Inhibition. Neuron 56, 33–42. https://doi.org/10.1016/j.neuron.2007.09.012

Guo, Z.V., Hires, S.A., Li, N., O'Connor, D.H., Komiyama, T., Ophir, E., Huber, D., Bonardi, C., Morandell, K., Gutnisky, D., Peron, S., Xu, N., Cox, J., Svoboda, K.,

2014. Procedures for Behavioral Experiments in Head-Fixed Mice. PLoS ONE 9, e88678. https://doi.org/10.1371/journal.pone.0088678
Hazan, L., Zugaro, M., Buzsáki, G., 2006. Klusters, NeuroScope, NDManager: A free software suite for neurophysiological data processing and visualization. J. Neurosci. Methods 155, 207–216. https://doi.org/10.1016/j.jneumeth.2006.01.017
Hirase, H., Czurkó, A., Csicsvari, J., Buzsáki, G., 1999. Firing rate and theta-phase coding by hippocampal pyramidal neurons during 'space clamping': Theta phase of hippocampal pyramidal cells. Eur. J. Neurosci. 11, 4373–4380. https://doi.org/10.1046/j.1460-9568.1999.00853.x
Klausberger, T., 2009. GABAergic interneurons targeting dendrites of pyramidal cells in the CA1 area of the hippocampus. Eur. J. Neurosci. 30, 947–957. https://doi.org/10.1111/j.1460-9568.2009.06913.x
Klausberger, T., Somogyi, P., 2008. Neuronal Diversity and Temporal Dynamics: The Unity of Hippocampal Circuit Operations. Science 321, 53–57. https://doi.org/10.1126/science.1149381
Korotkova, T., Fuchs, E.C., Ponomarenko, A., von Engelhardt, J., Monyer, H., 2010. NMDA Receptor Ablation on Parvalbumin-Positive Interneurons Impairs Hippocampal Synchrony, Spatial Representations, and Working Memory. Neuron 68, 557–569. https://doi.org/10.1016/j.neuron.2010.09.017
Kraus, B.J., Robinson, R.J., White, J.A., Eichenbaum, H., Hasselmo, M.E., 2013. Hippocampal "Time Cells": Time versus Path Integration. Neuron 78, 1090–1101. https://doi.org/10.1016/j.neuron.2013.04.015
Kvitsiani, D., Ranade, S., Hangya, B., Taniguchi, H., Huang, J.Z., Kepecs, A., 2013. Distinct behavioural and network correlates of two interneuron types in prefrontal cortex. Nature 498, 363–366. https://doi.org/10.1038/nature12176
Lee, S.-H., Marchionni, I., Bezaire, M., Varga, C., Danielson, N., Lovett-Barron, M., Losonczy, A., Soltesz, I., 2014. Parvalbumin-Positive Basket Cells Differentiate among Hippocampal Pyramidal Cells. Neuron 82, 1129–1144. https://doi.org/10.1016/j.neuron.2014.03.034
Maaten, L. van der, Hinton, G., 2008. Visualizing Data using t-SNE. J. Mach. Learn. Res. 9, 2579–2605.
MacDonald, C.J., Carrow, S., Place, R., Eichenbaum, H., 2013. Distinct Hippocampal Time Cell Sequences Represent Odor Memories in Immobilized Rats. J. Neurosci. 33, 14607–14616. https://doi.org/10.1523/JNEUROSCI.1537-13.2013
MacDonald, C.J., Lepage, K.Q., Eden, U.T., Eichenbaum, H., 2011. Hippocampal "Time Cells" Bridge the Gap in Memory for Discontiguous Events. Neuron 71, 737–749. https://doi.org/10.1016/j.neuron.2011.07.012
Mahn, M., Gibor, L., Patil, P., Cohen-Kashi Malina, K., Oring, S., Printz, Y., Levy, R., Lampl, I., Yizhar, O., 2018. High-efficiency optogenetic silencing with soma-targeted anion-conducting channelrhodopsins. Nat. Commun. 9, 4125. https://doi.org/10.1038/s41467-018-06511-8
Markus, E.J., Barnes, C.A., McNaughton, B.L., Gladden, V.L., Skaggs, W.E., 1994. Spatial information content and reliability of hippocampal CA1 neurons: Effects of visual input. Hippocampus 4, 410–421. https://doi.org/10.1002/hipo.450040404
Mau, W., Sullivan, D.W., Kinsky, N.R., Hasselmo, M.E., Howard, M.W., Eichenbaum, H., 2018. The Same Hippocampal CA1 Population Simultaneously Codes

Temporal Information over Multiple Timescales. Curr. Biol. 28, 1499-1508.e4. https://doi.org/10.1016/j.cub.2018.03.051
McNaughton, B.L., Barnes, C.A., Gerrard, J.L., Gothard, K., Jung, M.W., Knierim, J.J., Kudrimoti, H., Qin, Y., Skaggs, W.E., Suster, M., Weaver, K.L., 1996. Deciphering the hippocampal polyglot: the hippocampus as a path integration system. J. Exp. Biol. 199, 173–185. https://doi.org/10.1242/jeb.199.1.173
McNaughton, B.L., Battaglia, F.P., Jensen, O., Moser, E.I., Moser, M.-B., 2006. Path integration and the neural basis of the "cognitive map." Nat. Rev. Neurosci. 7, 663–678. https://doi.org/10.1038/nrn1932
Mizuseki, K., Diba, K., Pastalkova, E., Buzsáki, G., 2011. Hippocampal CA1 pyramidal cells form functionally distinct sublayers. Nat. Neurosci. 14, 1174–1181. https://doi.org/10.1038/nn.2894
Modi, M.N., Dhawale, A.K., Bhalla, U.S., 2014. CA1 cell activity sequences emerge after reorganization of network correlation structure during associative learning. eLife 3, e01982. https://doi.org/10.7554/eLife.01982
O'Keefe, J., Recce, M.L., 1993. Phase relationship between hippocampal place units and the EEG theta rhythm. Hippocampus 3, 317–330. https://doi.org/10.1002/hipo.450030307
Pachitariu, M., Steinmetz, N., Kadir, S., Carandini, M., Kenneth D., H., 2016. Kilosort: realtime spike-sorting for extracellular electrophysiology with hundreds of channels (preprint). Neuroscience. https://doi.org/10.1101/061481
Pastalkova, E., Itskov, V., Amarasingham, A., Buzsáki, G., 2008. Internally Generated Cell Assembly Sequences in the Rat Hippocampus. Science 321, 1322–1327. https://doi.org/10.1126/science.1159775
Prerau, M.J., Brown, R.E., Bianchi, M.T., Ellenbogen, J.M., Purdon, P.L., 2017. Sleep Neurophysiological Dynamics Through the Lens of Multitaper Spectral Analysis. Physiology 32, 60–92. https://doi.org/10.1152/physiol.00062.2015
Robinson, N.T.M., Priestley, J.B., Rueckemann, J.W., Garcia, A.D., Smeglin, V.A., Marino, F.A., Eichenbaum, H., 2017. Medial Entorhinal Cortex Selectively Supports Temporal Coding by Hippocampal Neurons. Neuron 94, 677-688.e6. https://doi.org/10.1016/j.neuron.2017.04.003
Royer, S., Zemelman, B.V., Losonczy, A., Kim, J., Chance, F., Magee, J.C., Buzsáki, G., 2012. Control of timing, rate and bursts of hippocampal place cells by dendritic and somatic inhibition. Nat. Neurosci. 15, 769–775. https://doi.org/10.1038/nn.3077
Salz, D.M., Tiganj, Z., Khasnabish, S., Kohley, A., Sheehan, D., Howard, M.W., Eichenbaum, H., 2016. Time Cells in Hippocampal Area CA3. J. Neurosci. 36, 7476–7484. https://doi.org/10.1523/JNEUROSCI.0087-16.2016
Schultheiss, N.W., Schlecht, M., Jayachandran, M., Brooks, D.R., McGlothan, J.L., Guilarte, T.R., Allen, T.A., 2020. Awake delta and theta-rhythmic hippocampal network modes during intermittent locomotor behaviors in the rat. Behav. Neurosci. 134, 529–546. https://doi.org/10.1037/bne0000409
Shimbo, A., Izawa, E.-I., Fujisawa, S., 2021. Scalable representation of time in the hippocampus. Sci. Adv. 7, eabd7013. https://doi.org/10.1126/sciadv.abd7013
Skaggs, W.E., McNaughton, B.L., Wilson, M.A., Barnes, C.A., 1996. Theta phase precession in hippocampal neuronal populations and the compression of

temporal sequences. Hippocampus 6, 149–172. https://doi.org/10.1002/(SICI)1098-1063(1996)6:2<149::AID-HIPO6>3.0.CO;2-K
Slomianka, L., Amrein, I., Knuesel, I., Sørensen, J.C., Wolfer, D.P., 2011. Hippocampal pyramidal cells: the reemergence of cortical lamination. Brain Struct. Funct. 216, 301–317. https://doi.org/10.1007/s00429-011-0322-0
Soltesz, I., Losonczy, A., 2018. CA1 pyramidal cell diversity enabling parallel information processing in the hippocampus. Nat. Neurosci. 21, 484–493. https://doi.org/10.1038/s41593-018-0118-0
Stark, E., Eichler, R., Roux, L., Fujisawa, S., Rotstein, H.G., Buzsáki, G., 2013. Inhibition-Induced Theta Resonance in Cortical Circuits. Neuron 80, 1263–1276. https://doi.org/10.1016/j.neuron.2013.09.033
Taxidis, J., Pnevmatikakis, E.A., Dorian, C.C., Mylavarapu, A.L., Arora, J.S., Samadian, K.D., Hoffberg, E.A., Golshani, P., 2020. Differential Emergence and Stability of Sensory and Temporal Representations in Context-Specific Hippocampal Sequences. Neuron 108, 984-998.e9. https://doi.org/10.1016/j.neuron.2020.08.028
Villette, V., Malvache, A., Tressard, T., Dupuy, N., Cossart, R., 2015. Internally Recurring Hippocampal Sequences as a Population Template of Spatiotemporal Information. Neuron 88, 357–366. https://doi.org/10.1016/j.neuron.2015.09.052
Wang, Y., Romani, S., Lustig, B., Leonardo, A., Pastalkova, E., 2015. Theta sequences are essential for internally generated hippocampal firing fields. Nat. Neurosci. 18, 282–288. https://doi.org/10.1038/nn.3904
Zacks, J.M., Speer, N.K., Swallow, K.M., Maley, C.J., 2010. The brain's cutting-room floor: segmentation of narrative cinema. Front. Hum. Neurosci. 4. https://doi.org/10.3389/fnhum.2010.00168

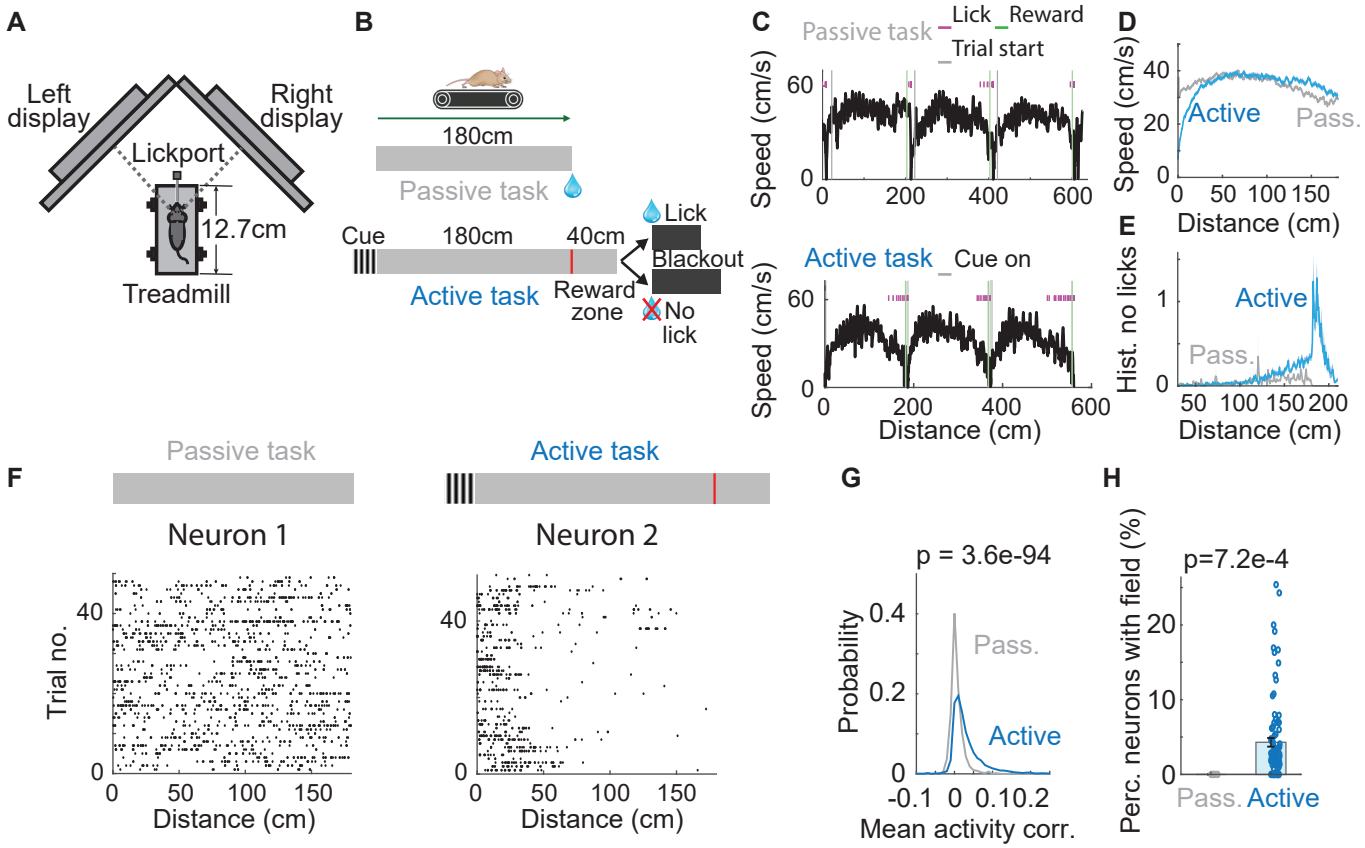
A
Left display
Right display
Lickport
12.7cm
Treadmill
B
180cm
Passive task
Cue
180cm
40cm
Active task
Reward zone
Lick
Blackout
No lick
C
Passive task
Lick
Reward
Trial start
Speed (cm/s)
Active task
Cue on
Distance (cm)
D
Active
Pass.
E
Hist. no licks
F
Passive task
Active task
Neuron 1
Neuron 2
Trial no.
G
p = 3.6e-94
Probability
Mean activity corr.
H
p=7.2e-4
Perc. neurons with field (%)

Figure 1

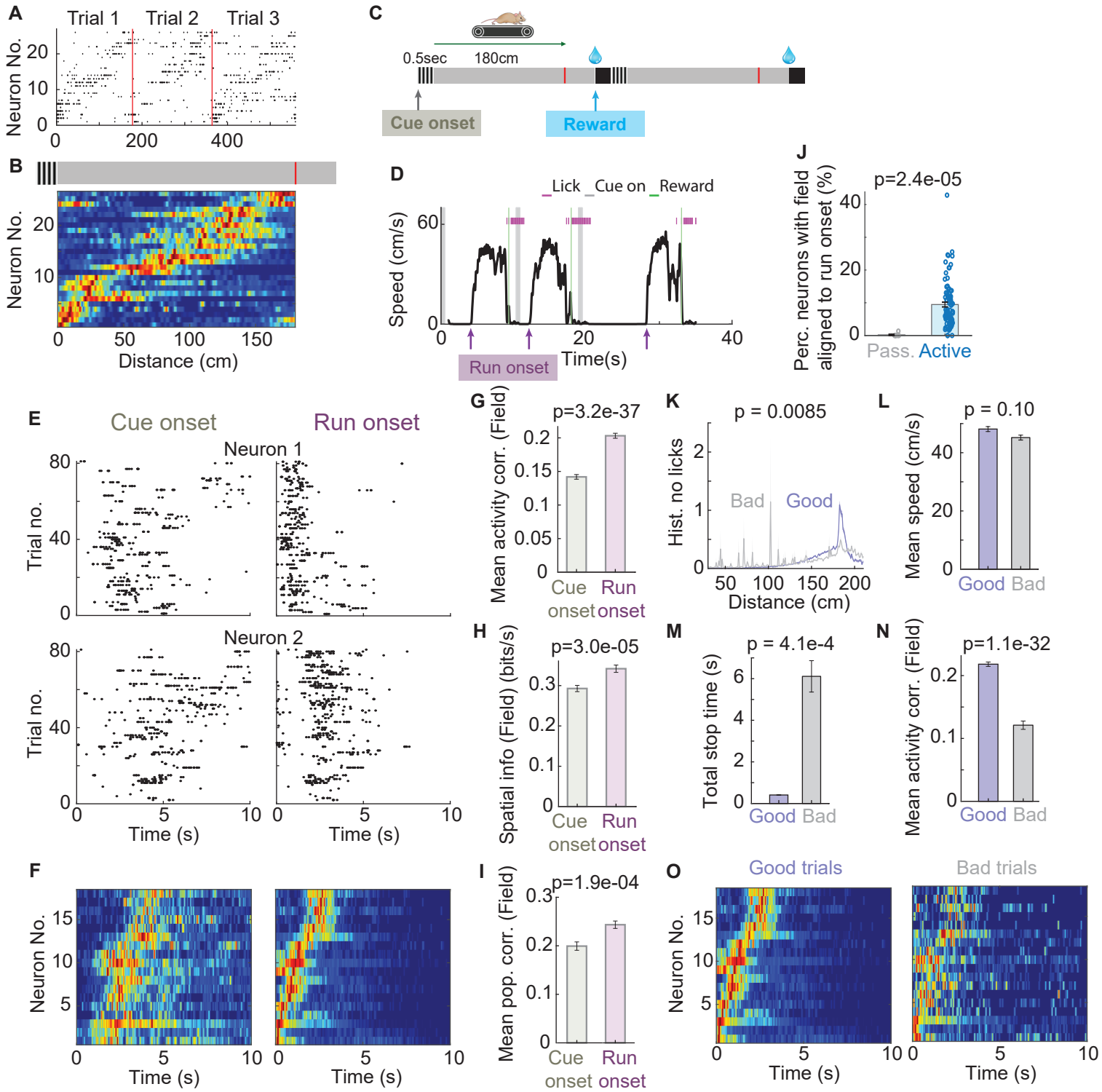
A
Trial 1
Trial 2
Trial 3
Neuron No.
B
Distance (cm)
C
0.5sec
180cm
Cue onset
Reward
D
Lick
Cue on
Reward
Speed (cm/s)
Run onset
Time(s)
E
Cue onset
Run onset
Neuron 1
Neuron 2
Trial no.
Time (s)
F
Neuron No.
Time (s)
G
p=3.2e-37
Mean activity corr. (Field)
Cue onset
Run onset
H
p=3.0e-05
Spatial info (Field) (bits/s)
I
p=1.9e-04
Mean pop. corr. (Field)
J
p=2.4e-05
Perc. neurons with field aligned to run onset (%)
Pass.
Active
K
p = 0.0085
Hist. no licks
Bad
Good
Distance (cm)
L
p = 0.10
Mean speed (cm/s)
M
p = 4.1e-4
Total stop time (s)
N
p=1.1e-32
O
Good trials
Bad trials

Figure 2

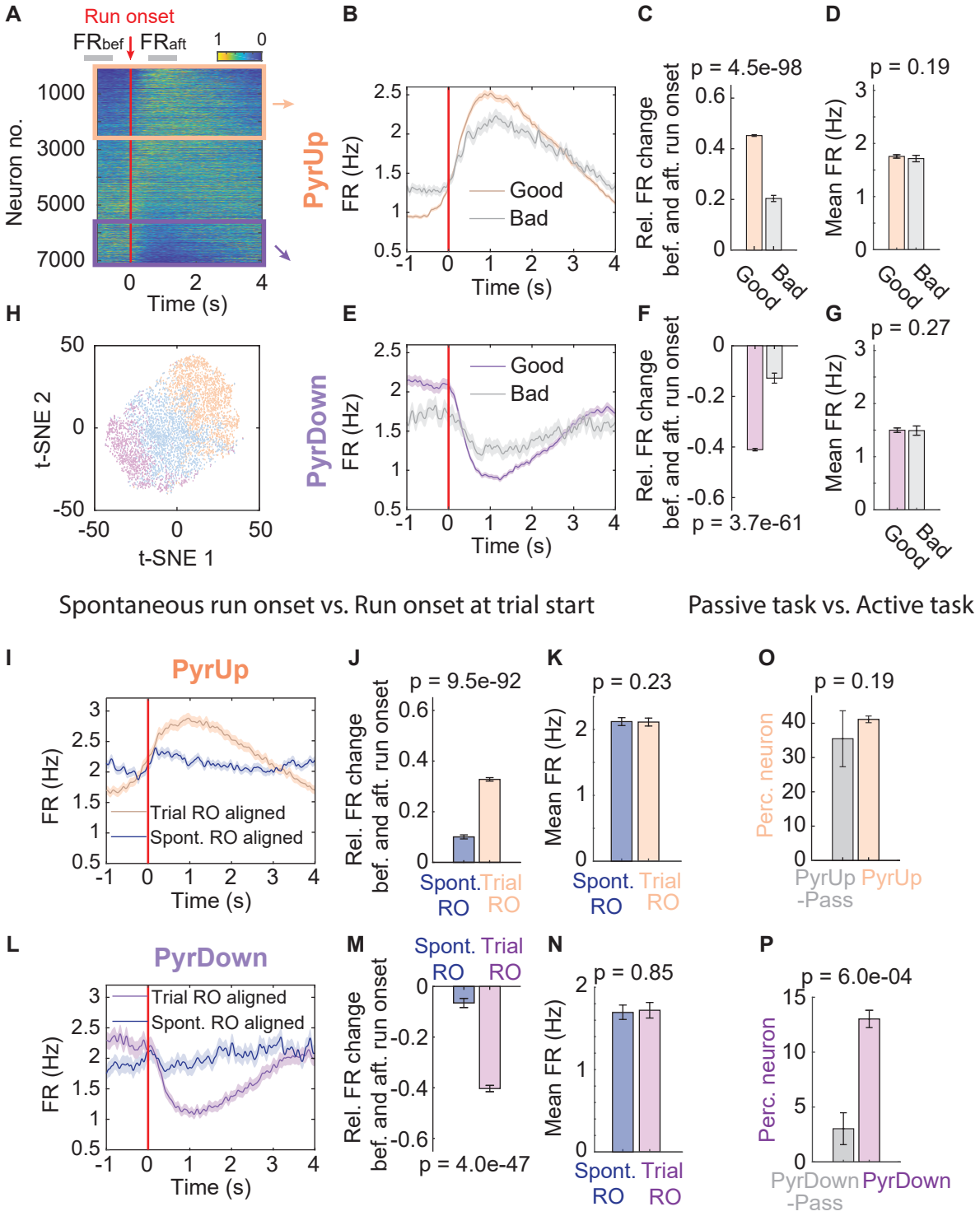
A
Run onset
FRbef
FRaft
1
0
Neuron no.
1000
3000
5000
7000
0
2
4
Time (s)
B
PyrUp
FR (Hz)
Good
Bad
Time (s)
C
p = 4.5e-98
Rel. FR change bef. and aft. run onset
Good
Bad
D
p = 0.19
Mean FR (Hz)
Good
Bad
H
t-SNE 2
t-SNE 1
E
PyrDown
FR (Hz)
Good
Bad
Time (s)
F
Rel. FR change bef. and aft. run onset
p = 3.7e-61
G
p = 0.27
Mean FR (Hz)
Good
Bad
Spontaneous run onset vs. Run onset at trial start
Passive task vs. Active task
I
PyrUp
FR (Hz)
Trial RO aligned
Spont. RO aligned
Time (s)
J
p = 9.5e-92
Rel. FR change bef. and aft. run onset
Spont. RO
Trial RO
K
p = 0.23
Mean FR (Hz)
Spont. RO
Trial RO
O
p = 0.19
Perc. neuron
PyrUp -Pass
PyrUp
L
PyrDown
FR (Hz)
Trial RO aligned
Spont. RO aligned
Time (s)
M
Spont. RO
Trial RO
Rel. FR change bef. and aft. run onset
p = 4.0e-47
N
p = 0.85
Mean FR (Hz)
Spont. RO
Trial RO
P
p = 6.0e-04
Perc. neuron
PyrDown -Pass
PyrDown

Figure 3

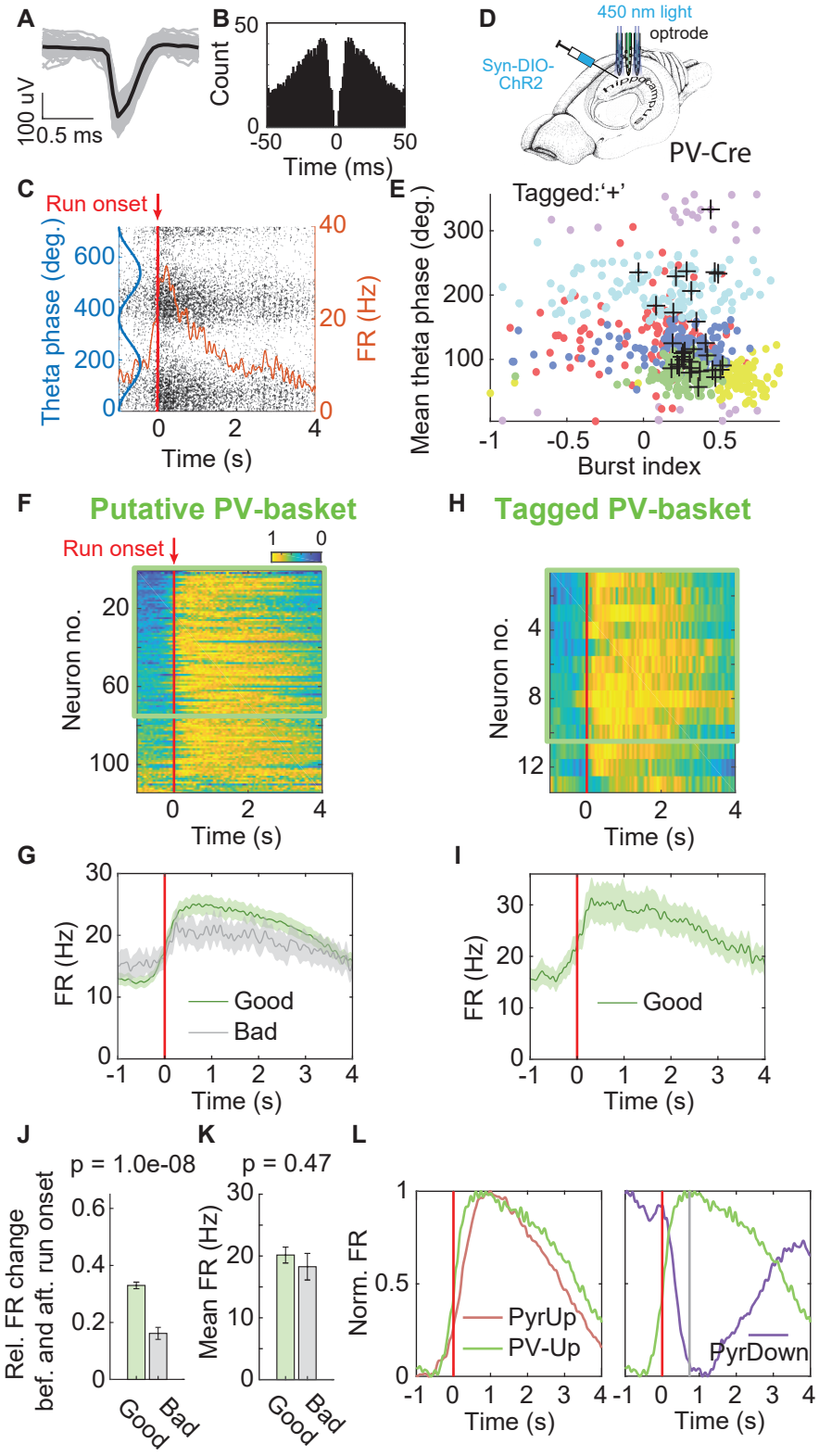
A
100 uV
0.5 ms
B
Count
50
0
-50
0
50
Time (ms)
D
450 nm light
optrode
Syn-DIO-ChR2
hippocampus
PV-Cre
C
Run onset
Theta phase (deg.)
600
400
200
0
40
20
0
FR (Hz)
0
2
4
Time (s)
E
Tagged:'+'
Mean theta phase (deg.)
300
200
100
-1
-0.5
0
0.5
Burst index
F
Putative PV-basket
Run onset
1
0
Neuron no.
20
60
100
0
2
4
Time (s)
H
Tagged PV-basket
Neuron no.
4
8
12
0
2
4
Time (s)
G
FR (Hz)
30
20
10
0
Good
Bad
-1
0
1
2
3
4
Time (s)
I
FR (Hz)
30
20
10
0
Good
-1
0
1
2
3
4
Time (s)
J
p = 1.0e-08
Rel. FR change bef. and aft. run onset
0.6
0.4
0.2
0
Good
Bad
K
p = 0.47
Mean FR (Hz)
30
20
10
0
Good
Bad
L
Norm. FR
1
0.5
0
PyrUp
PV-Up
-1
0
1
2
3
4
Time (s)
PyrDown
-1
0
1
2
3
4
Time (s)

Figure 4

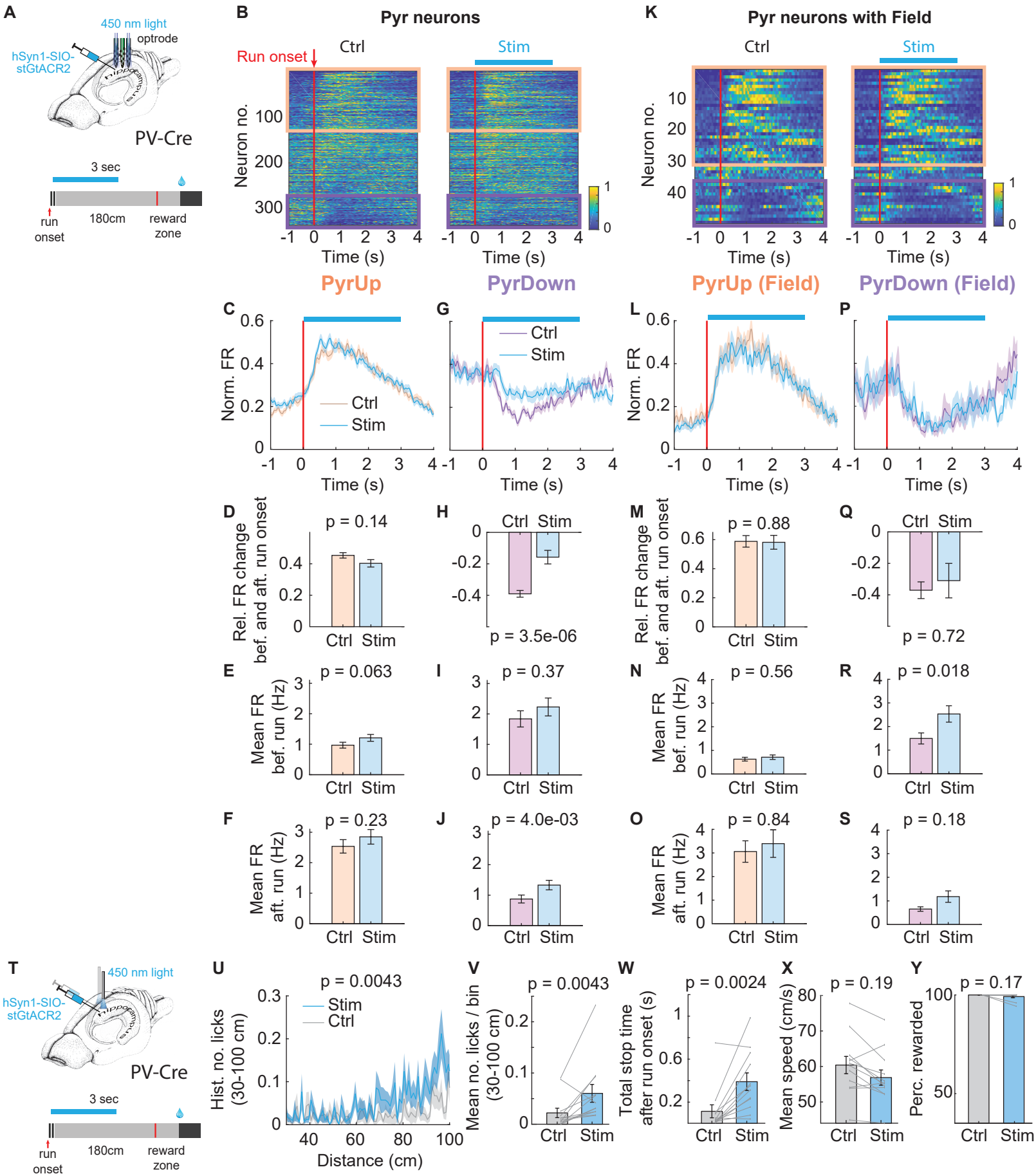
A
450 nm light
optrode
hSyn1-SIO-stGtACR2
PV-Cre
3 sec
run onset
180cm
reward zone
B
Pyr neurons
Ctrl
Stim
Run onset
Neuron no.
Time (s)
K
Pyr neurons with Field
PyrUp
PyrDown
PyrUp (Field)
PyrDown (Field)
Norm. FR
Rel. FR change bef. and aft. run onset
Mean FR bef. run (Hz)
Mean FR aft. run (Hz)
p = 0.14
p = 3.5e-06
p = 0.88
p = 0.72
p = 0.063
p = 0.37
p = 0.56
p = 0.018
p = 0.23
p = 4.0e-03
p = 0.84
p = 0.18
T
U
Hist. no. licks (30-100 cm)
Distance (cm)
p = 0.0043
V
Mean no. licks / bin (30-100 cm)
p = 0.0043
W
Total stop time after run onset (s)
p = 0.0024
X
Mean speed (cm/s)
p = 0.19
Y
Perc. rewarded
p = 0.17

Figure 5

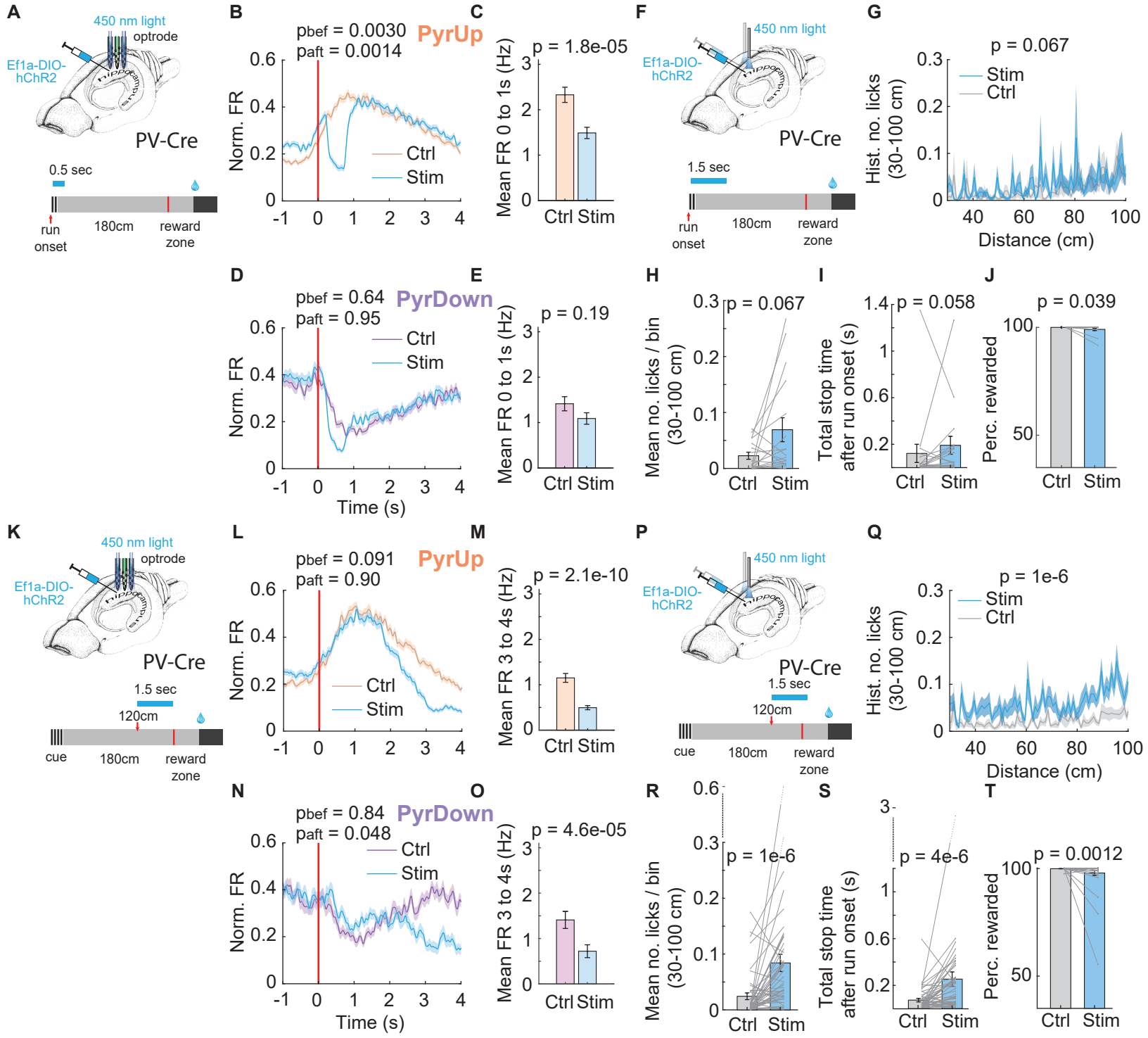
A
450 nm light
optrode
Ef1a-DIO-hChR2
PV-Cre
0.5 sec
run onset
180cm
reward zone
B
pbef = 0.0030
paft = 0.0014
PyrUp
Norm. FR
Ctrl
Stim
C
p = 1.8e-05
Mean FR 0 to 1s (Hz)
Ctrl Stim
F
450 nm light
Ef1a-DIO-hChR2
PV-Cre
1.5 sec
run onset
180cm
reward zone
G
p = 0.067
Stim
Ctrl
Hist. no. licks (30-100 cm)
Distance (cm)
D
pbef = 0.64
paft = 0.95
PyrDown
Norm. FR
Ctrl
Stim
Time (s)
E
p = 0.19
Mean FR 0 to 1s (Hz)
Ctrl Stim
H
p = 0.067
Mean no. licks / bin (30-100 cm)
Ctrl Stim
I
p = 0.058
Total stop time after run onset (s)
Ctrl Stim
J
p = 0.039
Perc. rewarded
Ctrl Stim
K
450 nm light
optrode
Ef1a-DIO-hChR2
PV-Cre
1.5 sec
120cm
cue
180cm
reward zone
L
pbef = 0.091
paft = 0.90
PyrUp
Norm. FR
Ctrl
Stim
M
p = 2.1e-10
Mean FR 3 to 4s (Hz)
Ctrl Stim
P
450 nm light
Ef1a-DIO-hChR2
PV-Cre
1.5 sec
120cm
cue
180cm
reward zone
Q
p = 1e-6
Stim
Ctrl
Hist. no. licks (30-100 cm)
Distance (cm)
N
pbef = 0.84
paft = 0.048
PyrDown
Norm. FR
Ctrl
Stim
Time (s)
O
p = 4.6e-05
Mean FR 3 to 4s (Hz)
Ctrl Stim
R
p = 1e-6
Mean no. licks / bin (30-100 cm)
Ctrl Stim
S
p = 4e-6
Total stop time after run onset (s)
Ctrl Stim
T
p = 0.0012
Perc. rewarded
Ctrl Stim

Figure 6

Active task depends on intact hippocampus

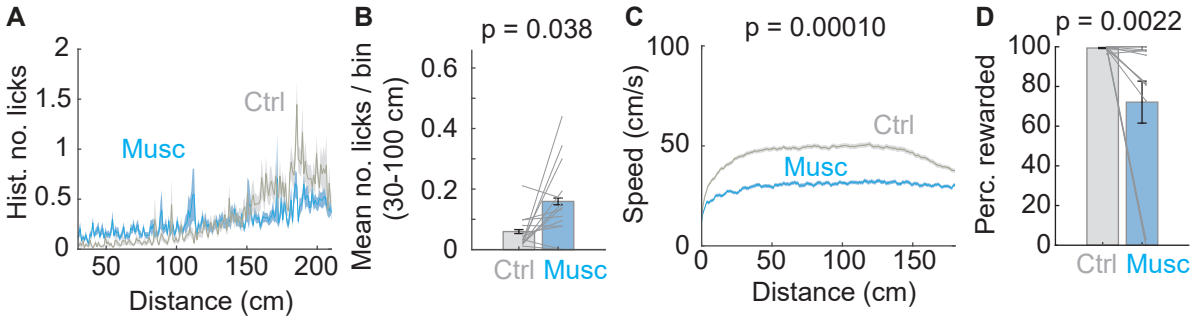

CA1 neuronal activity is better aligned to run onset

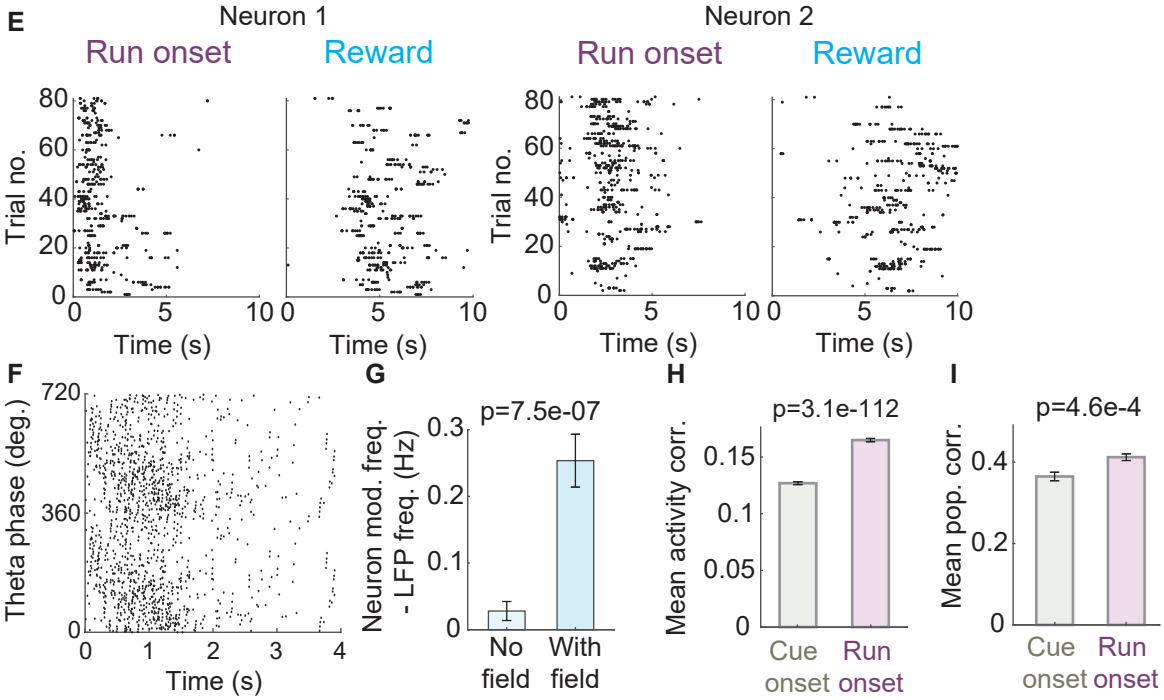

Brain state is maintained during the brief stop before run onset

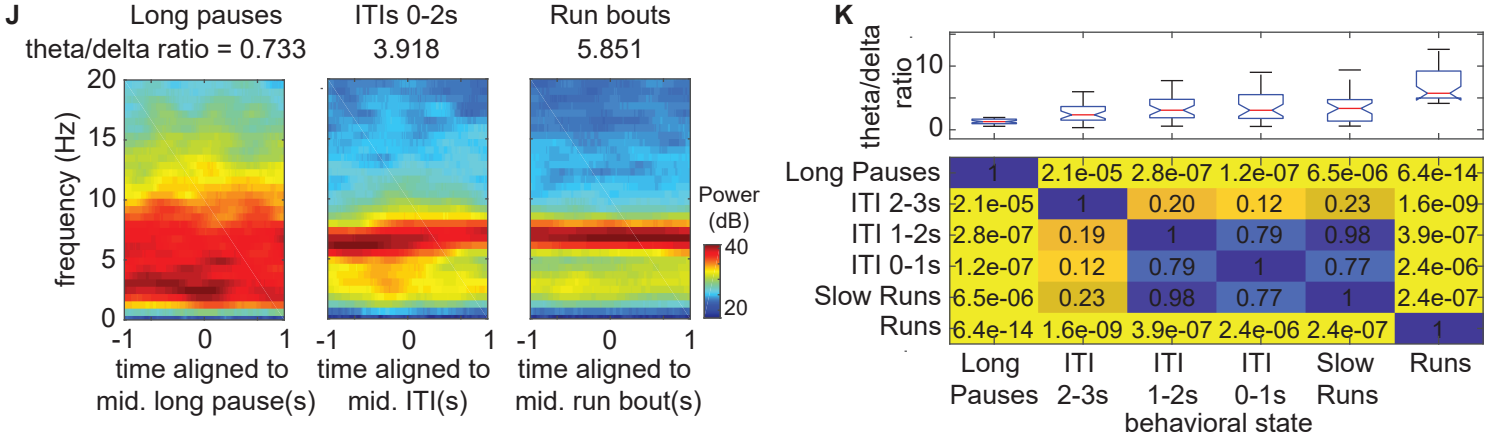

Proper run onset is necessary for accurate integration

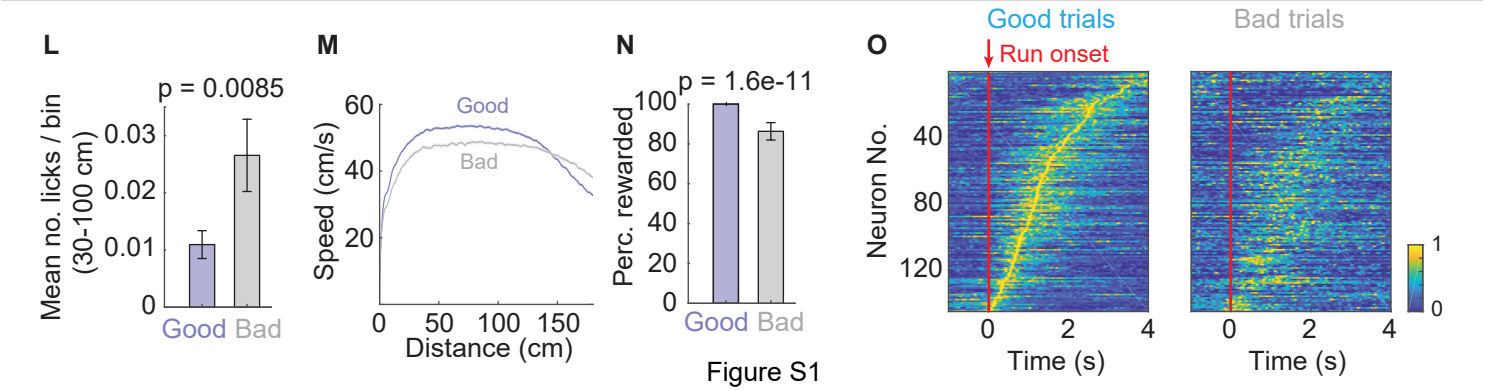

Figure S1

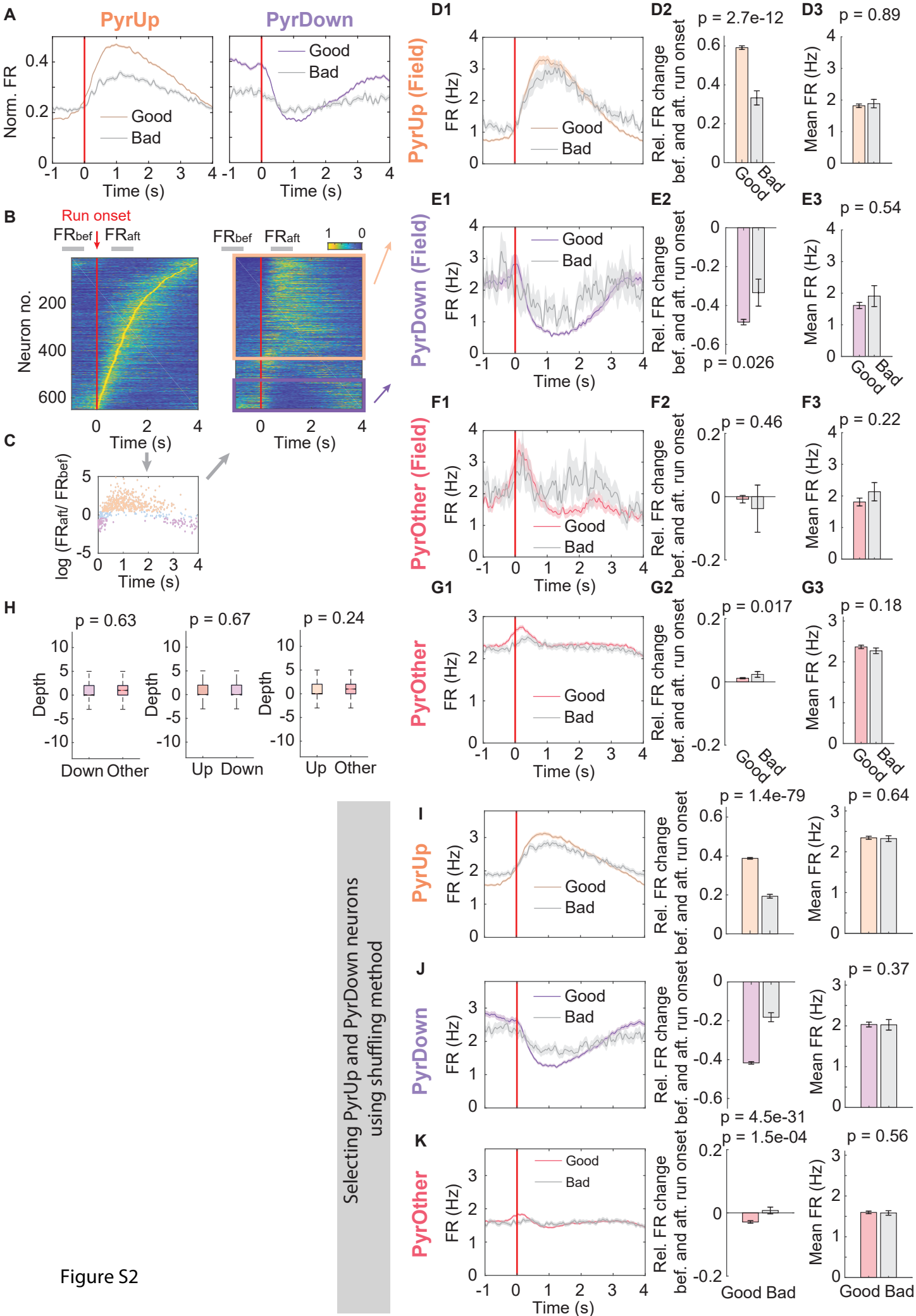
A
PyrUp
PyrDown
Norm. FR
Good
Bad
Time (s)
B
Run onset
FRbef
FRaft
Neuron no.
C
log (FRaft/ FRbef)
D1
D2
D3
PyrUp (Field)
p = 2.7e-12
p = 0.89
Rel. FR change bef. and aft. run onset
Mean FR (Hz)
FR (Hz)
E1
E2
E3
PyrDown (Field)
p = 0.026
p = 0.54
F1
F2
F3
PyrOther (Field)
p = 0.46
p = 0.22
G1
G2
G3
PyrOther
p = 0.017
p = 0.18
H
p = 0.63
p = 0.67
p = 0.24
Depth
Down Other
Up Down
Up Other
Selecting PyrUp and PyrDown neurons using shuffling method
I
PyrUp
p = 1.4e-79
p = 0.64
J
PyrDown
p = 4.5e-31
p = 0.37
K
PyrOther
p = 1.5e-04
p = 0.56

Figure S2

PyrUp and PyrDown responses are specific to run onset at the trial start in the active task

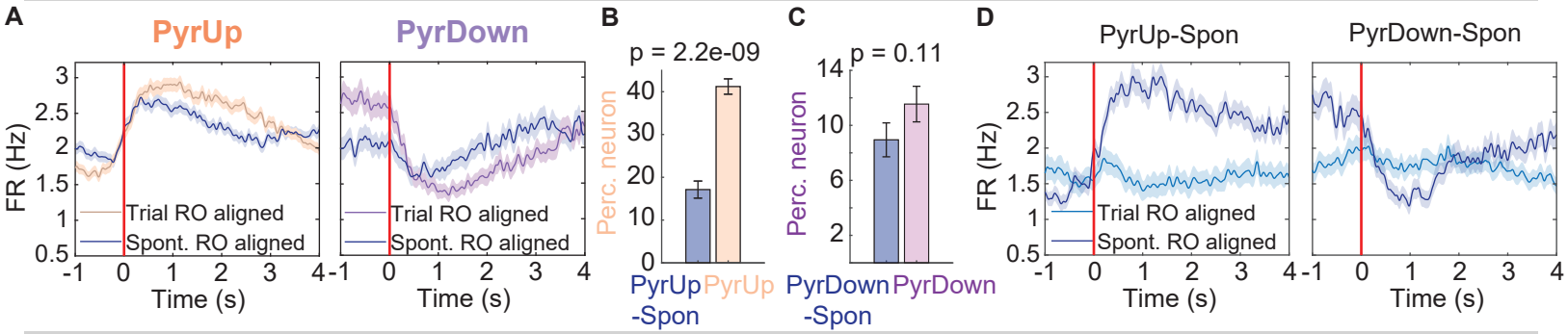

Percentage of PyrDown neurons is low in the passive task

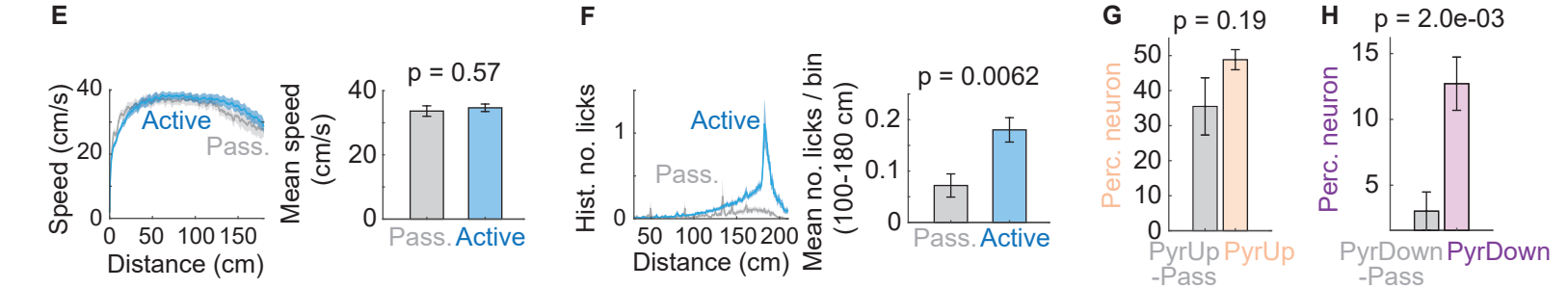

PyrUp and PyrDown responses in an immobile task.

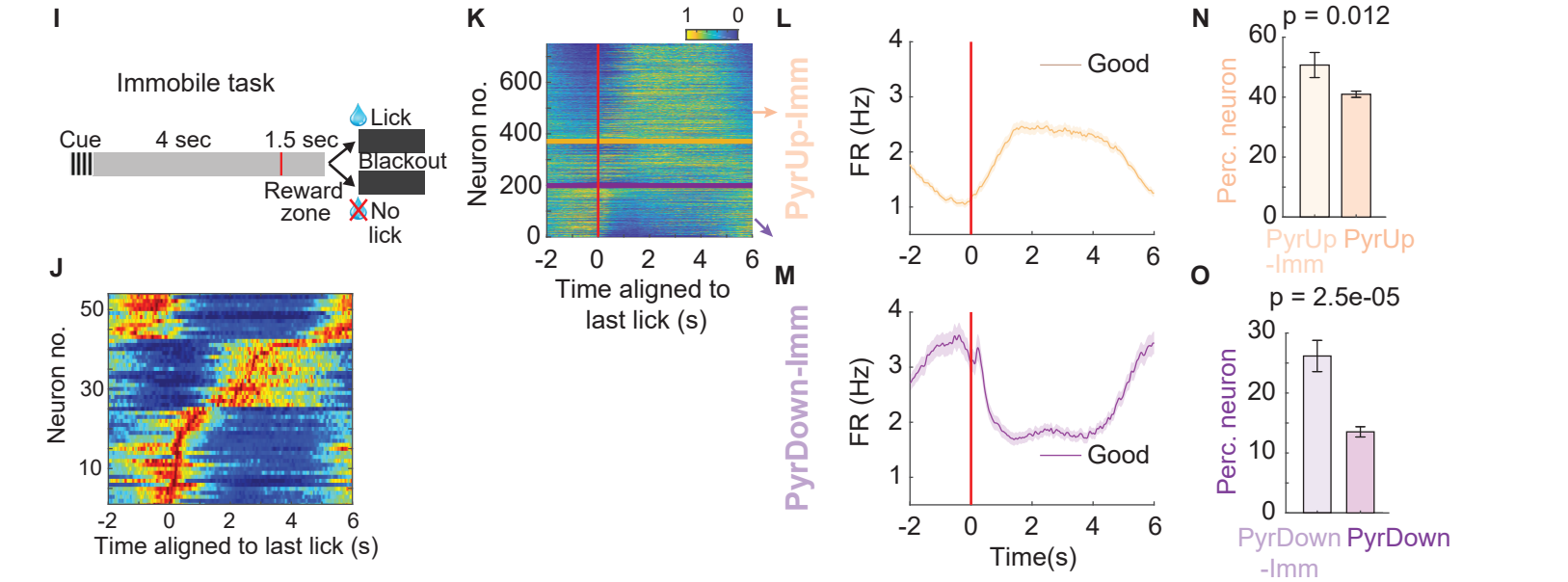

Tagging of PV-tasket cells

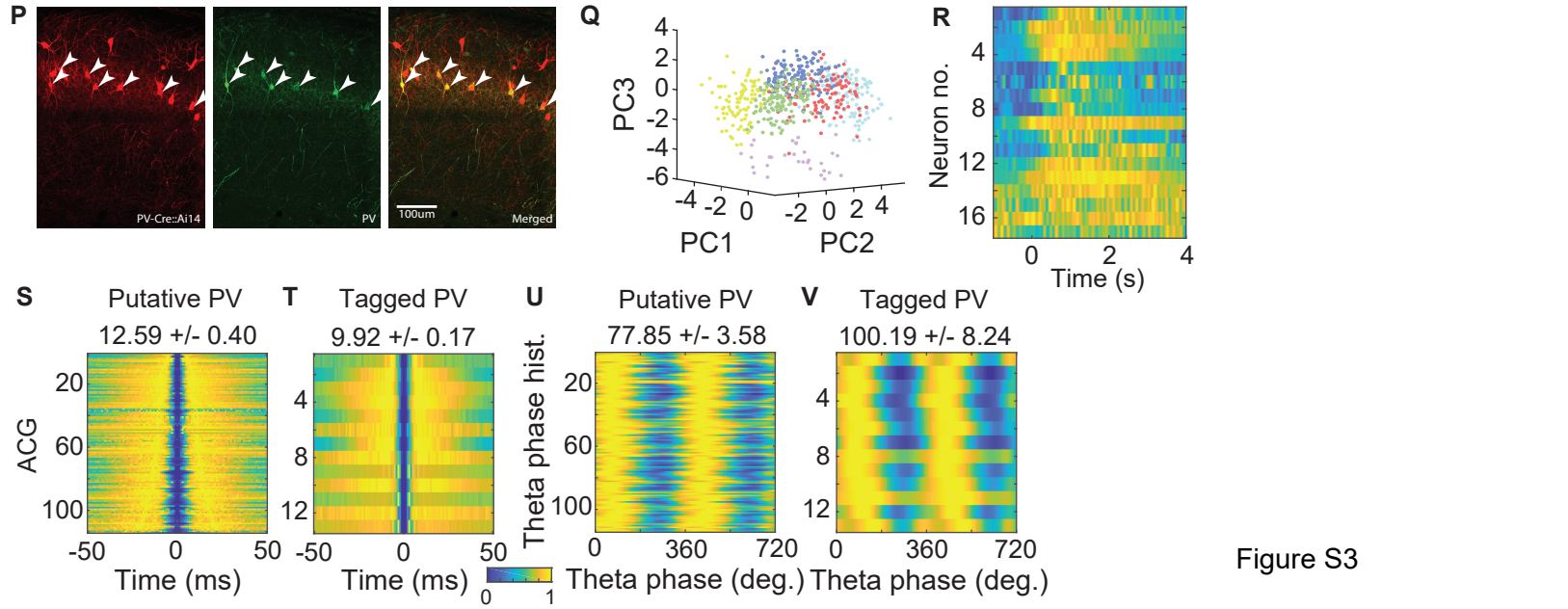

Figure S3

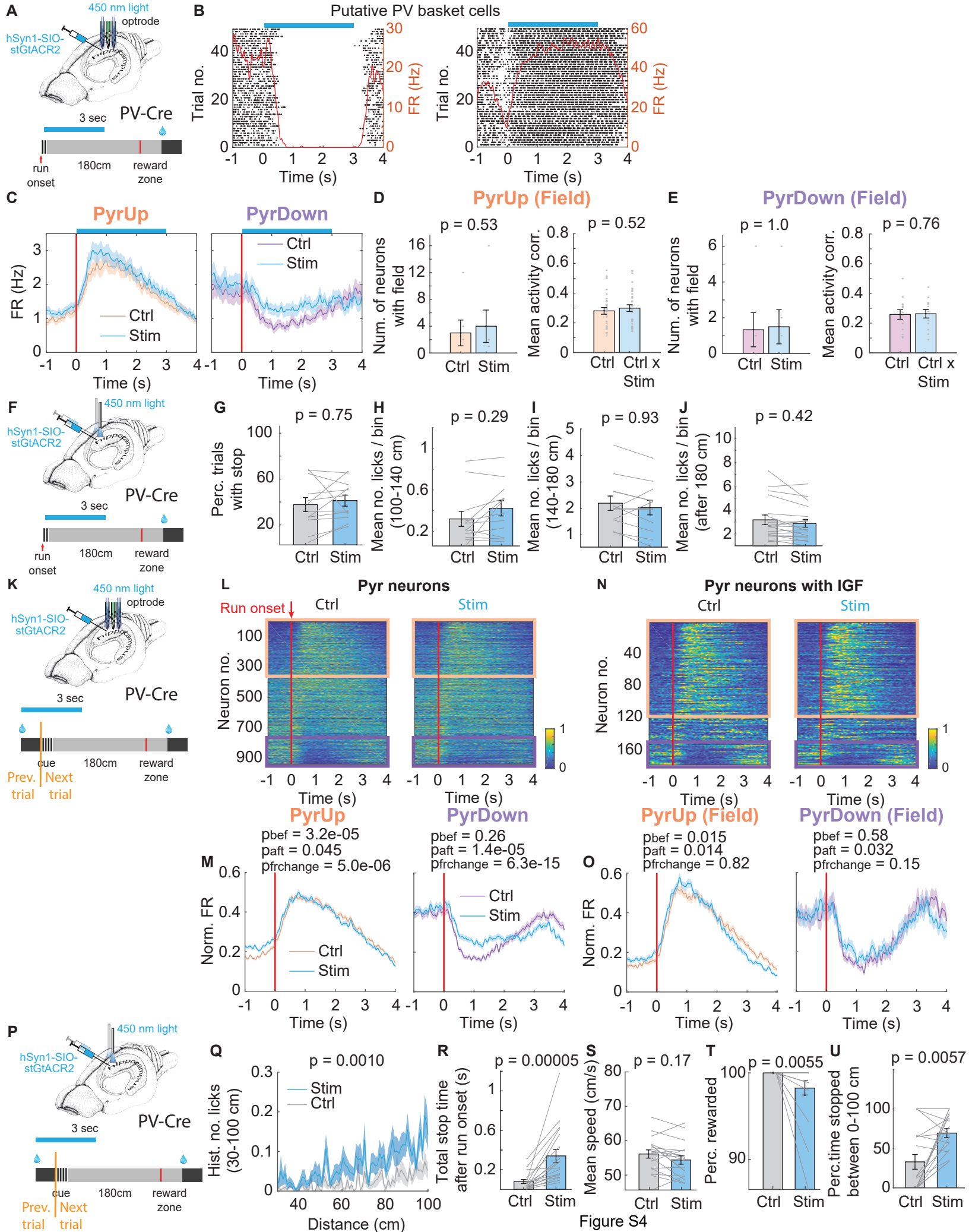
A
450 nm light
optrode
hSyn1-SIO-stGtACR2
hippocampus
PV-Cre
3 sec
run onset
180cm
reward zone
B
Putative PV basket cells
Trial no.
FR (Hz)
Time (s)
C
PyrUp
PyrDown
FR (Hz)
Ctrl
Stim
Time (s)
D
PyrUp (Field)
p = 0.53
p = 0.52
Num. of neurons with field
Mean activity corr.
Ctrl
Stim
Ctrl x Stim
E
PyrDown (Field)
p = 1.0
p = 0.76
F
G
p = 0.75
Perc. trials with stop
H
p = 0.29
Mean no. licks / bin (100-140 cm)
I
p = 0.93
Mean no. licks / bin (140-180 cm)
J
p = 0.42
Mean no. licks / bin (after 180 cm)
K
cue
Prev. trial
Next trial
L
Pyr neurons
Run onset
Neuron no.
N
Pyr neurons with IGF
M
PyrUp
pbef = 3.2e-05
paft = 0.045
pfrchange = 5.0e-06
PyrDown
pbef = 0.26
paft = 1.4e-05
pfrchange = 6.3e-15
Norm. FR
O
PyrUp (Field)
pbef = 0.015
paft = 0.014
pfrchange = 0.82
PyrDown (Field)
pbef = 0.58
paft = 0.032
pfrchange = 0.15
P
Q
p = 0.0010
Hist. no. licks (30-100 cm)
Distance (cm)
R
p = 0.00005
Total stop time after run onset (s)
S
p = 0.17
Mean speed (cm/s)
T
p = 0.0055
Perc. rewarded
U
p = 0.0057
Perc.time stopped between 0-100 cm

Figure S4

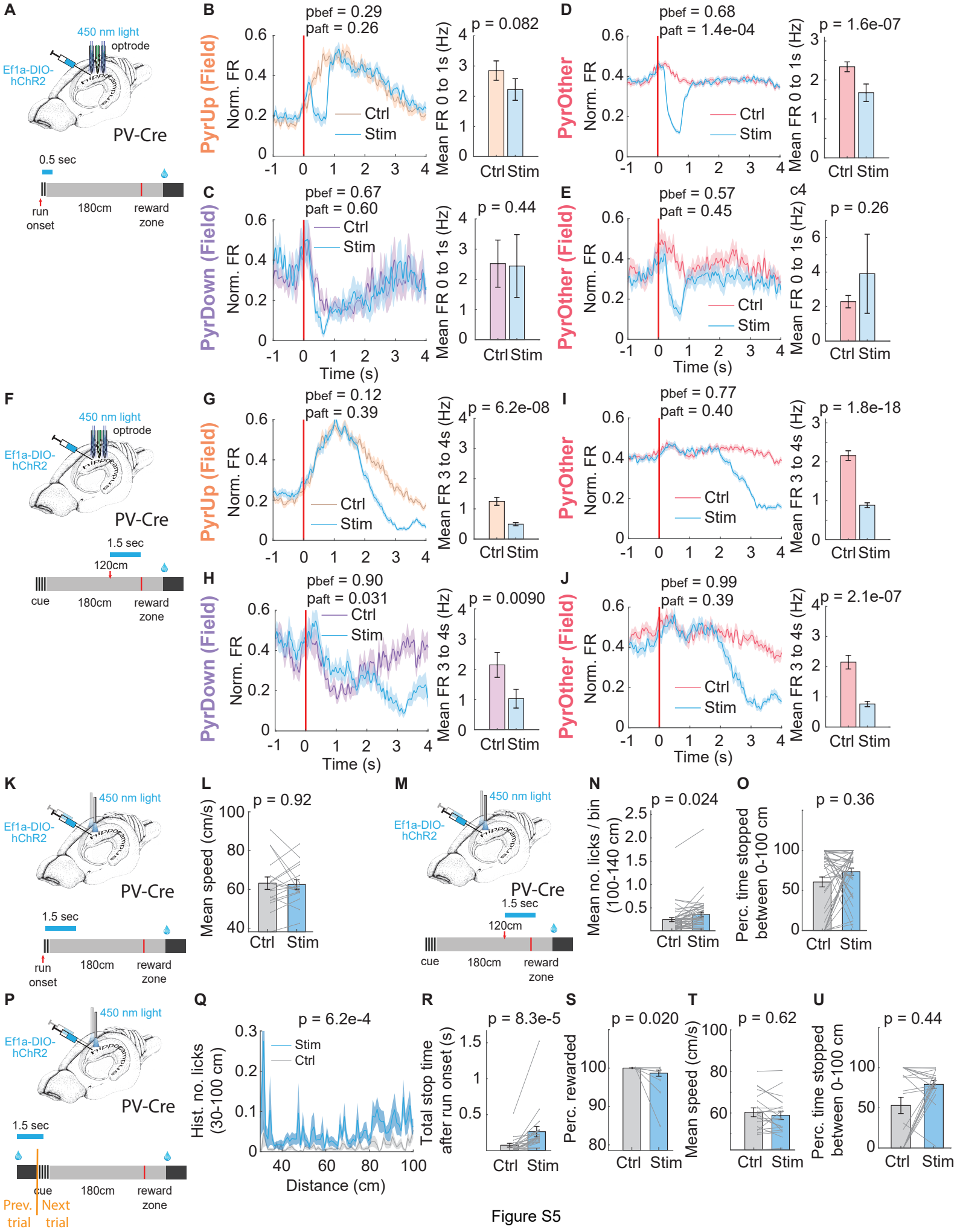
A
450 nm light
optrode
Ef1a-DIO-hChR2
PV-Cre
0.5 sec
run onset
180cm
reward zone
B
pbef = 0.29
paft = 0.26
p = 0.082
PyrUp (Field)
Norm. FR
Ctrl
Stim
Mean FR 0 to 1s (Hz)
D
pbef = 0.68
paft = 1.4e-04
p = 1.6e-07
PyrOther
C
pbef = 0.67
paft = 0.60
p = 0.44
PyrDown (Field)
Time (s)
E
pbef = 0.57
paft = 0.45
p = 0.26
F
450 nm light
optrode
Ef1a-DIO-hChR2
PV-Cre
1.5 sec
120cm
cue
180cm
reward zone
G
pbef = 0.12
paft = 0.39
p = 6.2e-08
Mean FR 3 to 4s (Hz)
I
pbef = 0.77
paft = 0.40
p = 1.8e-18
H
pbef = 0.90
paft = 0.031
p = 0.0090
J
pbef = 0.99
paft = 0.39
p = 2.1e-07
K
450 nm light
Ef1a-DIO-hChR2
PV-Cre
1.5 sec
run onset
180cm
reward zone
L
p = 0.92
Mean speed (cm/s)
M
450 nm light
Ef1a-DIO-hChR2
PV-Cre
1.5 sec
120cm
cue
180cm
reward zone
N
p = 0.024
Mean no. licks / bin (100-140 cm)
O
p = 0.36
Perc. time stopped between 0-100 cm
P
450 nm light
Ef1a-DIO-hChR2
PV-Cre
1.5 sec
cue
180cm
reward zone
Prev. trial
Next trial
Q
p = 6.2e-4
Hist. no. licks (30-100 cm)
Distance (cm)
R
p = 8.3e-5
Total stop time after run onset (s)
S
p = 0.020
Perc. rewarded
T
p = 0.62
Mean speed (cm/s)
U
p = 0.44
Perc. time stopped between 0-100 cm

Figure S5

Bayesian decoding using PyrUp and PyrDown neurons without IGFs

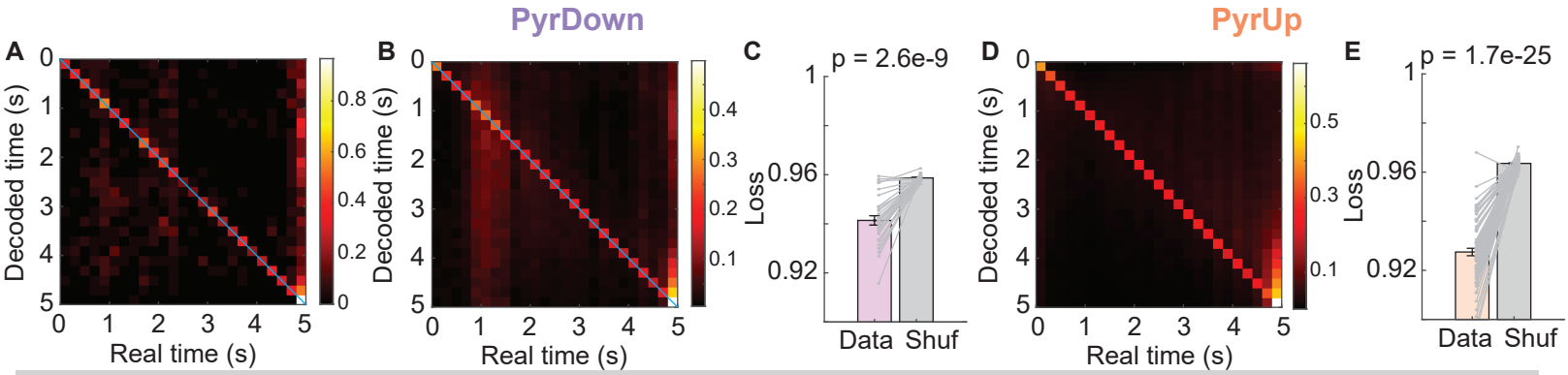

Peak detection for PyrUp and PyrDown neurons

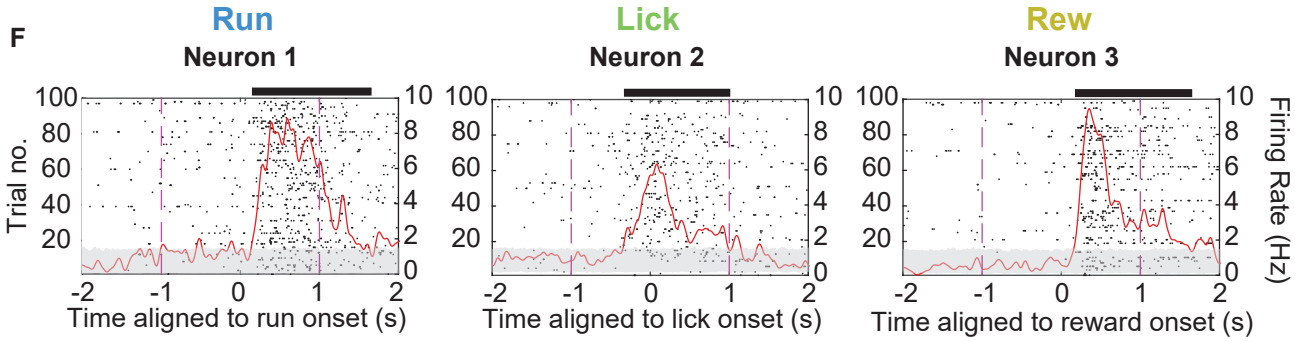

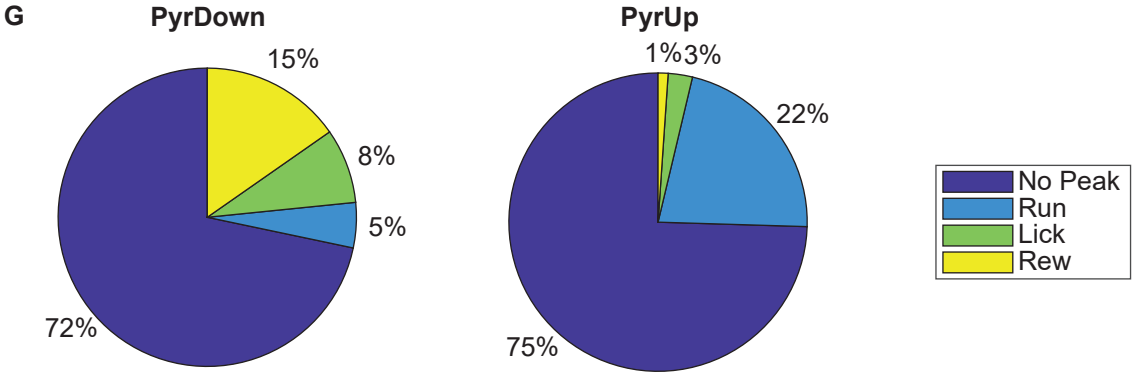

Optogenetic inactivation control

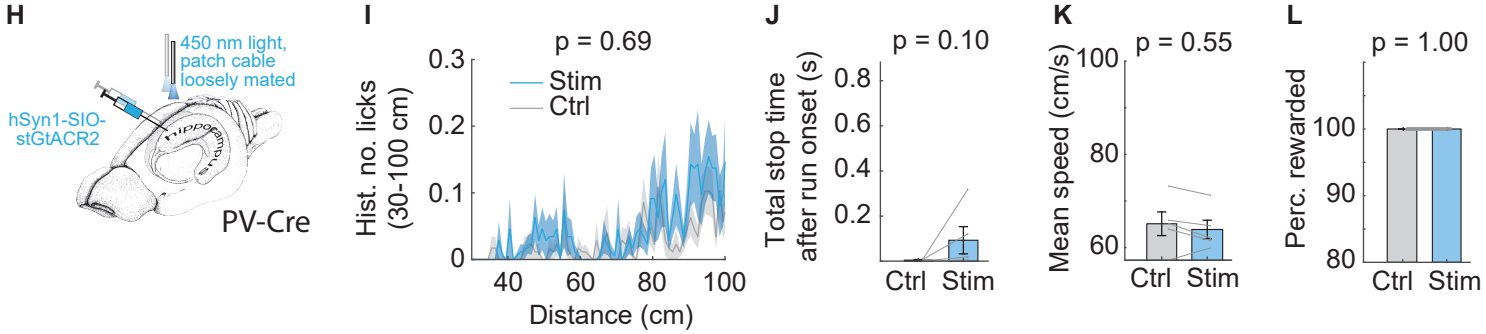

Optogenetic activation control

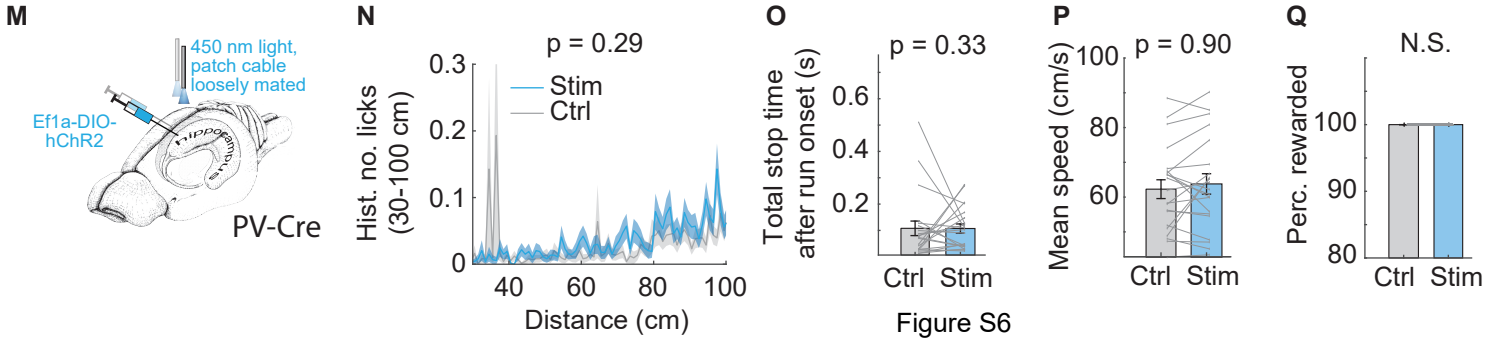

Figure S6